Timescales of ultra-high temperature metamorphism and crustal differentiation: Zircon petrochronology from granulite xenoliths of the Variscan French Massif Central

Oscar Laurent, Simon Couzinié, Luc Doucet

Timescales of ultra-high temperature metamorphism and crustal differentiation: zircon petrochronology from granulite xenoliths of the Variscan French Massif Central

Oscar Laurent[1,2], Simon Couzinié[3,4], Luc. S Doucet[5]

[1]*CNRS, Géosciences Environnement Toulouse, Observatoire Midi-Pyrénées, 14 avenue Edouard Belin, 31400 Toulouse, France*

[2]*ETH Zürich, Institute for Geochemistry and Petrology, Clausiusstrasse 25, 8092 Zürich, Switzerland*

[3]*Université de Lorraine, CNRS, CRPG, 54000 Nancy, France*

[4]*Université de Lyon, ENS de Lyon, Université Lyon 1, CNRS, UMR 5276 LGL-TPE, 69342 Lyon, France*

[5]*Earth Dynamics Research Group, TIGeR, Curtin University, 6845 Perth, WA, Australia*

Abstract

Lower crustal ultra-high temperature (UHT) metamorphism and the resulting production and transfer of granitic magmas represent key processes of intracrustal differentiation. The timescales of these phenomena are debated, due to the complexity of the granulite zircon U-Pb record and because direct links between granulites and granites are difficult to establish. To address these issues, we present the results of zircon petrochronology (coupled U-Pb dating, trace element and Lu-Hf isotopic analyses) for lower crustal felsic and mafic granulite xenoliths from the Variscan eastern French Massif Central and compare them with data from well-characterized mid-/upper crustal migmatites and granites. The felsic and mafic granulites represent pre-Variscan meta-sedimentary and meta-igneous mafic rocks, respectively; which experienced Variscan UHT peak metamorphism at 940–970 °C and 8 ± 2 kbar. Zircons from the felsic granulites show U-Pb dates spreading over ~50 Myr between ~315 and ~265 Ma, correlated to Ti-in-zircon temperatures decreasing from 940–970 °C to 800 °C and REE contents consistent with growth in equilibrium with garnet at (U)HT conditions. This is best explained by continuous crystallization of zircon upon cooling from the thermal peak owing to decreasing Zr solubility of residual melt, despite significant prograde melt loss. Zircons from the mafic granulite only record the last stage of this time-temperature evolution (295–265 Ma;

800–900 °C) due to later zircon saturation. Upper crustal granite emplacement started at 340 Ma and culminated at the age of the lower crustal thermal peak of 313 ± 3 Ma (defined by the highest-temperature zircons from felsic granulites), reflecting melt extraction along the ~27 Myr prograde path of the lower crust. In turn, the crystallization ages of mid-crustal migmatites (315–300 Ma) and the lower crustal granulites (315–265 Ma) are consistent with slow cooling in the presence of melt. These results provide a direct assessment of the timescales of melt production and residence at the crustal scale; and validate the granulite-granite connection in the framework of the melt loss theory in migmatitic systems.

Keywords: UHT metamorphism; partial melting; crustal differentiation; granulite; zircon; Variscan orogeny

1. Introduction

The formation and differentiation of the Earth's continental crust is a two-step process. New crust produced mainly in magmatic arcs (e.g. Collins et al., 2020; Jagoutz and Klein, 2018) is reworked during orogenic events through tectonic, metamorphic and/or magmatic processes to produce the continental crust with bulk andesitic composition and layered structure (Cawood et al., 2013; Hacker et al., 2015; Rudnick and Gao, 2014). In particular, (ultra-)high-temperature [(U)HT], granulite-facies metamorphism and partial melting of the lower crust, followed by the segregation and ascent of the resulting granitic magmas, is a key process of intracrustal differentiation (Harley, 2016; Moyen et al., 2017a; Sawyer et al., 2011; Zheng and Gao, 2021). Mid- to upper crustal granitic plutons and lower crustal granulites would represent the two complementary products of this process i.e., the extracted magma and residual solid respectively (Brown, 2013; Cawood et al., 2013; Clemens et al., 1990, 2020; Vielzeuf et al., 1990; White and Powell, 2002). This concept has been validated by phase equilibria modelling (White et al., 2001; Yakymchuk and Brown, 2014a), experimental petrology (Gao et al., 2016) and the investigation of melt inclusions in metamorphic minerals (Cesare et al., 2009).

Melt segregation and extraction from the lower crust can theoretically happen at the melt connectivity threshold of 5 to 7 vol.% (Rabinowicz and Vigneresse, 2004; Rosenberg and Handy, 2005). Therefore, melt loss is expected to occur progressively as it is produced along

the prograde P–T path of the lower crust (Brown, 2013; Kelsey and Hand, 2015; White and Powell, 2002; Yakymchuk and Brown, 2014a). Because melt segregation and transport are geologically fast (<100 kyr and down to <1 kyr in duration; Harris et al. 2000; Petford et al., 2000; Scaillet et al., 2006), granite formation should pre-date or at least be synchronous with the lower crustal (U)HT metamorphic peak. However, this hypothesis has not been systematically tested yet, mainly because direct links between granulites and granites are difficult to establish as these represent two different paleo-crustal levels.

Moreover, even when a field connection between granulites and granites is made possible by tectonic reworking or the presence of lower crustal xenoliths, the comparison is entangled by the complex geochronological record of granulites. Zircon U-Pb dates in granulites commonly span several 10s to 100s of Myr (Kelly and Harley, 2005; Kelsey and Hand, 2015; Harley, 2016; Harley and Black, 1987; Taylor et al., 2016 and references therein). Interpretations of this protracted zircon record vary from pulsed mineral growth in response to metamorphic reactions along different parts of the P–T path (Baldwin et al., 2007; Hermann and Rubatto, 2003; Rubatto et al., 2013; Vavra et al., 1996); continuous crystallization through melt Zr saturation upon cooling (Guergouz et al., 2018; Kelsey et al., 2008; Taylor et al., 2015a); igneous crystallization in the case of mafic granulites (Costa and Rey, 1995; Moyen et al., 2017b); or even post-crystallization disturbance of the U-Pb system (Taylor et al., 2014; Kunz et al., 2018).

In this context, better understanding the processes and timescales of crustal differentiation requires to (i) robustly assess the significance of zircon U-Pb dates in lower crustal granulites; and (ii) directly compare these with the age and origin of co-genetic, mid-/upper crustal granite plutons. For this purpose, we present here the results of zircon petrochronology (coupled U-Pb dating, trace element quantification and Lu-Hf isotopic analyses) from lower crustal felsic and mafic granulite xenoliths of the Variscan eastern French Massif Central (E-FMC). These are interpreted to record (U)HT metamorphism, partial melting and magmatic underplating related to the late stages of the Variscan orogeny (Downes and Leyreloup, 1986; Downes et al., 1990; Costa and Rey, 1995; Leyreloup et al., 1977), whose mid- to upper crustal expression is well constrained from the study of exposed migmatites and granites (Barbey et al., 1999; Laurent et al., 2017; Montel et al., 1992; Moyen et al., 2017a; Villaros et al., 2018, Williamson et al., 1997). They provide therefore an ideal case study to investigate the nature of the

parameters controlling U-Pb age distributions in granulites; and how such distribution relates to melt production in, and extraction from the lower crust to eventually differentiate the crust.

2. Crustal history and structure of the eastern French Massif Central

The E-FMC is part of the Variscan Belt of Western Europe. The E-FMC crust consists of Ediacaran (605–555 Ma) sedimentary rocks (now paragneisses) deposited in a back-arc basin along the northern Gondwana margin which were intruded by igneous rocks (now orthogneisses) during back-arc inversion in the late Ediacaran–Cambrian (545–525 Ma) and subsequent Ordovician (485–450 Ma) extension (Chelle-Michou et al., 2017; Couzinié et al., 2017, 2019). These lithologies were reworked in the Devonian–Carboniferous through metamorphism and magmatism, associated with convergence and collision between Laurussia and Gondwana (see review in Vanderhaeghe et al., 2020). Cenozoic rifting was associated with abundant alkaline volcanism that peaked in Miocene–Pliocene times (Michon and Merle, 2001).

This study focuses on the area of the Velay migmatite-granite dome in the E-FMC (Fig. 1a). The local metamorphic rocks belong to several nappes (Vanderhaeghe et al., 2020): (i) the allochtonous Upper Gneiss Unit, typified by a bimodal meta-igneous association at its base (the so-called “Leptynite-Amphibolite complex”) and a Devonian HP-HT metamorphic evolution; (ii) the Lower Gneis Unit, composed of upper amphibolite-facies, migmatitic ortho- and paragneisses devoid of HP record; (iii) the Paurautochtonous Unit, comprising lower-grade metasediments. Migmatitic rocks from the Lower Gneiss Unit define a broad structural dome ~100 km in diameter (Ledru et al., 2001), decorated by 340–310 Ma granite massifs/dykes and cored by the 310–300 Ma Velay diatexite and associated granites (Montel et al., 1992; Chelle-Michou et al., 2017; Didier et al., 2013; Laurent et al., 2017) (Fig. 1a). Petrological and geochemical data demonstrate that most 340–310 Ma granites were sourced in the lower crust (Downes et al., 1997; Villaros et al., 2018). In contrast, the 310–300 Ma Velay diatexite and granites formed from both the accumulation of lower crustal melts/magmas and anatectic melts formed nearly *in situ* at mid-crustal depths, largely at the expense of orthogneisses (Montel et al., 1992; Williamson et al., 1997; Barbey et al., 1999; Chelle-Michou et al., 2017; Villaros et al., 2018; Couzinié et al., 2021).

The studied xenolith suite originates from the Bournac site (Fig. 1a) where they are hosted in a phreatomagmatic breccia pipe of Upper Miocene age (Couthures et al., 1991). The basaltic breccia contains numerous enclaves of amphibolite- to granulite-facies crustal rocks (Leyreloup et al., 1977). The granulite-facies xenoliths reached peak metamorphic conditions of up to 6–15 kbar and 800–1000°C (Fig. 1b, Dostal et al., 1980; Downes and Leyreloup, 1986; Leyreloup, 1992) and were thus interpreted as sampling the lower crust (Leyreloup, 1992). Among these, two distinct lithologies were identified by previous studies: (i) mafic granulites, of igneous origin (47%); (ii) felsic granulites corresponding to meta-sedimentary (42%) or meta-igneous rocks (11%) (Costa and Rey, 1995; Dostal et al., 1980; Downes et al., 1990; Downes and Leyreloup, 1986; Leyreloup, 1992; Leyreloup et al., 1977).

Whole-rock Nd model ages of the granulite xenoliths range from 1.0 to 1.8 Ga (Downes and Leyreloup, 1986; Downes et al., 1990), similar to those of exposed Variscan rocks in the FMC (Downes et al., 1997). Published geochronology includes thermal ionization mass spectrometry (TIMS) U-Pb dating of monazite and zircon that yielded a dominant 320–280 Ma range in both meta-sedimentary and mafic meta-igneous xenoliths, interpreted as reflecting granulite-facies metamorphism and coeval crystallization of underplated basaltic magmas, respectively (Costa and Rey, 1995; Downes et al., 1990). Further secondary ion mass spectrometry (SIMS) zircon U-Pb dating in a meta-sedimentary granulite revealed two populations of Neoproterozoic to early Paleozoic, detrital grains (630–430 Ma) and Carboniferous to Permian (360–250 Ma) metamorphic grains (Rossi et al., 2006).

The Bournac xenoliths would sample the lower crust formed during the Variscan orogeny and underwent minimal disturbance since then (Costa and Rey, 1995; Downes and Leyreloup, 1986; Downes et al., 1990), notably as this crust segment remained less affected by Tethyan oceanization than other Variscan domains like Corsica (Rossi et al., 2006) or the Ivrea Zone (Guergouz et al., 2018). The felsic granulites would represent lower crustal residues after extraction of magmas that rose and accumulated in mid-crustal migmatite units and upper crustal, peraluminous granite bodies (Fig. 1b) (Vanderhaeghe et al., 2020; Villaros et al., 2018). The mafic meta-igneous rocks are generally interpreted as under/intraplated mantle-derived magmas (Costa and Rey, 1995; Downes et al., 1990) or alternatively as a constituent lithology of the local pre-Variscan crust (Dostal et al., 1980; Downes and Leyreloup, 1986).

3. Materials and methods

We have investigated two meta-sedimentary, felsic granulites (HS15-BOU01 and HS15-BOU17) and one meta-igneous, mafic granulite (HS15-BOU07). These were selected on petrological and geochemical grounds as to be best representative of the two dominant lithological groups identified among the lower crustal xenoliths throughout the French Massif Central (see sections 2 and 4.1). We have worked on zircon separates instead of directly on thin sections as to provide a statistically meaningful dataset for each sample. For this purpose, we targeted samples among the largest xenoliths (spheroids 10–15 cm in diameter), which allowed to analyze 80 to 142 grains per sample (in comparison, thin sections contain about 10 useable grains). After sawing out the outermost 2–3 cm-thick edge of the samples, affected by interactions with the host (Leyreloup, 1992), the innermost part was selected for thin section preparation and $\gtrsim$ 500 g powdered down to <80 µm for bulk rock elemental analysis. The remaining material was crushed and sieved to <500 µm for heavy mineral separation. Zircon grains were concentrated using standard techniques (panning, magnetic and heavy liquids separation, handpicking), cast in epoxy resin and polished down to a sub-equatorial section.

Bulk rock major and trace element compositions were determined at the Service d'Analyse des Roches et des Minéraux (CNRS–CRPG, Nancy, France). Major element compositions of minerals were measured in thin sections by electron microprobe analysis using a CAMECA SX100 instrument at Service Microsonde Sud (Université Montpellier 2, France). Thin section cathodoluminescence imaging was performed using a "cold-cathode" Technosyn 8200 Mk2 at CEREGE (Marseille, France) and a "hot-cathode" Lumic HC6-LM at GET (Toulouse, France). Zircon cathodoluminescence imaging was performed at the Laboratoire Magmas et Volcans (Clermont-Ferrand, France) using a Jeol JSM-5910 scanning electron microscope. Simultaneous zircon U-Pb dating and trace element analyses were carried out at ETH Zürich (ETHZ), Switzerland, by laser ablation – inductively coupled plasma – mass spectrometry (LA-ICP-MS) using a RESOlution S-155 (ASI, Australia) 193 nm (ArF) excimer laser system coupled to an Element XR (Thermo Scientific, Germany) sector-field ICP-MS. Analyses of Lu-Hf isotopes in zircon were performed by by laser ablation – multi-collection – inductively coupled plasma – mass spectrometry (LA-MC-ICP-MS) at ETHZ using the same laser ablation system as for U-Pb dating and trace elements, attached to a Nu Plasma 2 (Nu Instruments, UK) MC-ICP-MS. Garnet and rutile trace element data were

obtained by LA-ICP-MS at the Service ICP-MS of Observatoire Midi-Pyrénées in Toulouse (France), using a NWRfemto (ESI, USA) solid-state laser ablation system coupled to an Element XR sector-field ICP-MS. Phase equilibrium modelling was undertaken using the software Perple_X (version 6.9.1, Nov. 2021, Connolly, 2009) in the system Na_2O–CaO–K_2O–FeO–MgO–Al_2O_3–SiO_2–H_2O–TiO_2(–O_2), i.e. NCKFMASHT(O).

Details about the analytical and modelling procedures are provided in the Supplementary Material. The data on samples and reference materials are provided in the Data Tables.

4. Results

4.1. Petrography and geochemistry

Felsic granulites HS15-BOU-01 and HS15-BOU-17 (Fig. 2a,b) are composed of a seriate interlobate to polygonal assemblage of quartz (15–25 vol.%), plagioclase ($An_{30-38}Ab_{52-60}Or_{9-16}$; 20–28 vol.%), slightly perthitic alkali feldspar ($An_{1-5}Ab_{24-33}Or_{63-74}$; 25–32 vol.%), chemically unzoned garnet ($alm_{51-56}pyr_{39-45}grs_4sps_{0-1}$; 22–27 vol.%) (Supplementary Figures S1 and S2) and prismatic sillimanite, which occurs associated with plagioclase in HS15-BOU-17 (making up 5–6 vol.% of the rock) and only as inclusions within garnet in HS15-BOU-01. Both hand specimens exhibit mm-scale banding with alternating plagioclase vs. alkali feldspar–quartz layers (Fig. 2). Accessory minerals are rutile, apatite, and zircon. Zircon is mainly located at grain boundaries and rarely as inclusion in garnet (Fig. 2). Whole-rock compositions match those of meta-sedimentary granulite xenoliths from the E-FMC (Fig. 3a,b). The felsic granulites are selectively enriched in Fe, Mg, Ti and depleted in alkalis at a given SiO_2 content with respect to lower-grade metasediments of the local crust (Fig. 3a,b), which likely results from melt loss during anatexis (Leyreloup et al., 1977). The same hypothesis was proposed to explain similar chemical differences between granulite-facies (“stronalites”, to which our samples are akin, Fig. 3) and amphibolite-facies (“kinzigites”) meta-sediments from the deep crustal section of the Ivrea-Verbano Zone, NW Italy (Redler et al., 2013; Schnetger, 1994). From a trace element perspective, the felsic granulites are chemically complementary to peraluminous granites from the E-FMC (Fig. 3c).

Mafic granulite sample HS15-BOU-07 consists of a granoblastic assemblage of plagioclase (~60 vol.%), orthopyroxene (~22 vol.%), clinopyroxene (~14 vol.%), ilmenite (~2 vol.%) with accessory apatite and zircon, the latter being either included in major minerals (most often plagioclase) or located along grain boundaries. Both ortho- and clinopyroxene grains appear corroded by a microcrystalline, dark-coloured (in plane-polarized light), Fe-rich but alkali-free alteration rim, possibly representing a former melt film that infiltrated the xenolith. Whole-rock geochemical data indicate that the xenolith has a quartz-normative, basic (51.7 wt.% SiO_2), Al-rich (17.9 wt.% Al_2O_3) and K_2O-poor (0.3 wt.%) composition, lacks typical features of igneous cumulates (e.g. positive Eu anomaly) and shows an affinity to calc-alkaline suites (Fig. 3c). Such composition is consistent with that of a high-Al basaltic liquid (Crawford et al., 1987). These characteristics make HS15-BOU-07 representative of the most common group (~70%) of mafic granulites in the E-FMC (Dostal et al., 1980; Downes et al., 1990).

The lower crustal origin of the three xenoliths is supported by their high V_p values of 6.5–6.9 $km.s^{-1}$ (calculation procedure in the Supplementary Material), matching those of the lowermost crust (6.5–6.8 $km.s^{-1}$ at 20–28 km depth) in the E-FMC based on seismic data (Perrier and Ruegg, 1973).

4.2. Thermobarometry and phase equilibrium modelling

The results of pseudosection modelling indicate that the dry (biotite-free), mineralogy of felsic granulite samples entails temperatures >840°C, while the coexistence of garnet, sillimanite and rutile constrains pressures between 6.5 and 10–13 kbar (Fig. 1d and Supplementary Figure S3). It is worth noting that solidus temperatures are about 200 °C higher than the wet solidus of fertile meta-sedimentary rocks. This observation and the preservation of dry mineral assemblages imply that the rocks have experienced significant melt loss (Redler et al., 2013; White and Powell, 2002), which is in line with bulk-rock geochemistry (see section 4.1 and Fig. 3). Conventional thermobarometry yields equilibration conditions of 825 ± 29°C at 7.8 ± 0.5 kbar and 833 ± 11°C at 6.9 ± 0.7 kbar for HS15-BOU01 and HS15-BOU17, respectively (calculated with the two-feldspar thermometer of Putirka, 2008, and the GASP barometer of Holdaway, 2001, quoted “internal” uncertainties correspond to 2 standard deviations [SD]). The pressure estimated for HS15-BOU01 must be regarded as a minimum

as sillimanite is only present as inclusions in garnet, hence possibly not in equilibrium with matrix plagioclase. These conditions fall on the solidus for both samples.

Based on the calculated pseudosection, the absence of garnet and amphibole in mafic granulite HS15-BOU07 indicates temperatures exceeding 820°C for maximum pressures of 8.5–10 kbar (Fig. 1d). Quartz is predicted in low modal amounts (<4 vol.%) at such conditions but was not observed in thin section. The two-pyroxene thermobarometer of Putirka (2008) yielded temperature–pressure conditions of 904 ± 20°C and 9.4 ± 1.4 kbar which although affected by large uncertainties are consistent with pseudosection analysis.

4.3. Zircon data

In all three samples, zircon forms transparent, yellowish to colorless crystals ranging in size from 50 to 350 µm. In felsic granulites, they generally show rounded, nearly equant shapes, with the exception of a few elongated grains (Fig. 4a,b). Crystals are more irregularly shaped to anhedral in mafic granulite HS15-BOU07 (Fig. 4c). Two main zircon domains are identified based on CL images (Fig. 4): (i) entire grains or, more frequently, rounded cores showing well-developed zoning, most commonly oscillatory in felsic granulites and patchy in the mafic granulite; and (ii) entire grains or rims mantling the former, generally showing brighter, homogeneous luminescence and no to weak zoning. The cores show characteristics of resorbed zircon with internal zoning clearly truncated by irregular boundaries, which are either sharp or consist of a dark-CL seam, generally <10 µm- but up to 50 µm-thick (Fig. 4). Wherever visible, internal structures in the CL-bright, homogeneous rims and grains consist of sector, fir-tree and/or radial zoning, imparting a multifaceted ("soccerball") texture (Fig. 4). The volume ratio between homogeneous rims/grains and zoned cores/grains varies from a grain to another but, at the scale of the sample, homogeneous rims/grains dominate.

The results of LA-(MC-)ICP-MS analyses reveal clear differences between zoned cores/grains and homogeneous rims/grains, in terms of U-Pb dates, Hf isotopic ratios and trace element composition. In all samples, zoned cores/grains show a spread of mainly (sub-) concordant U-Pb dates (Fig. 5). In mafic granulite HS15-BOU07, most analyses (7 out of 11) range from Ordovician to Carboniferous (481 ± 9 to 307 ± 7 Ma) with a few younger spots and define a trend of decreasing $\varepsilon Hf_{(t)}$ with time from +5.0 at ~480 Ma to -2.3 at ~180 Ma (Fig. 6a). Zoned cores/grains in felsic granulites show dates mainly from Neoproterozoic to Permian (807

± 25 to 249 ± 8 Ma) (Fig. 5) and a wide range of $\varepsilon Hf_{(t)}$ between +5 and -16 (Fig. 6a), with few outliers at very negative values (down to -58). In contrast, homogeneous rims/grains in all samples show more clustered, Carboniferous to Permian U-Pb dates between 320 and 270 Ma (Fig. 5) with an apparent mode at 280–290 Ma. The $\varepsilon Hf_{(t)}$ values are also more homogeneous in a given sample than results from zoned cores/grains (Fig. 6a), with negative values in felsic granulites from -10.0 ± 3.3 (2 S.D.; n = 55) in HS15-BOU17 to -5.7 ± 3.0 (2 S.D.; n = 43) for HS15-BOU01; and positive values of +4.1 ± 1.2 (2 S.D.; n = 54) in mafic granulite HS15-BOU07.

While most zoned cores/grains show Ti contents between 10 and 35 ppm regardless their U-Pb date (Fig. 6b), homogeneous rims/grains have on average higher Ti (20–70 ppm). In felsic granulite samples, homogeneous rims/grains show a clear correlation between Ti content and U-Pb date, with >300 Ma spots having >50 ppm Ti, decreasing to 20–30 ppm at 260–280 Ma (Fig. 6b). Data from the mafic granulite do not show such correlation, yet overlap with the trend defined by homogeneous rims/grains in felsic granulites, at 270–300 Ma and 25–40 ppm Ti (Fig. 6b). In all samples, zoned cores/grains show more scattered and generally higher concentrations of most trace elements (Nb, Y, HREE, U, Th) than homogeneous rims/grains (Fig. 7). In felsic granulites the latter are further characterized by flat HREE profiles (Gd_N/Yb_N ~1) and pronounced negative Eu anomalies (Eu_N/Eu^* <0.1) compared with zoned cores/grains (Gd_N/Yb_N <0.2 and Eu_N/Eu^* ~0.05–1) (Fig. 7), as well as less pronounced positive Ce anomalies (Supplementary Figure S7).

In all samples, single homogeneous rims/grains analyzed multiple times generally show identical U-Pb dates and Hf isotopic ratios within uncertainties (Fig. 4), as well as only modest variations in trace element contents. Whenever analyzable, dark seams separating cores and rims show U-Pb dates and elemental/isotopic compositions that are similar to those of the rims (see examples from HS15-BOU07 in Fig. 4) and are therefore considered together with homogeneous rims/grains in the following.

5. Discussion

5.1. Zircon petrochronology of the Bournac granulites

5.1.1. Felsic granulites

316 The dichotomy between zoned cores/grains vs. homogeneous grains/rims is typical of
317 zircon from (U)HT felsic granulites and reflects inheritance from the protolith vs. metamorphic
318 growth (Kelly and Harley, 2005; Kunz et al., 2018; Taylor et al., 2016; Vavra et al., 1996). The
319 range of inherited U-Pb ages is consistent with a former detrital zircon population. This range
320 is skewed towards younger (mainly Paleozoic) ages (Fig. 5) compared with the detrital zircon
321 age distribution in exposed meta-sedimentary rocks in the E-FMC, showing a Neoproterozoic
322 (550–800 Ma) peak (Chelle-Michou et al., 2017; Couzinié et al., 2019), certainly reflecting Pb
323 loss during the Variscan (U)HT event (see Supplementary Figure S8). The crystallization of
324 homogeneous rims/grains during Variscan metamorphism is confirmed by U-Pb dates
325 overlapping with the Carboniferous to early Permian age of this event in the E-FMC (review in
326 Vanderhaeghe et al., 2020) and their distinctive trace element signature, in line with that of
327 metamorphic zircon from (U)HT granulites (Fig. 7) (e.g. Kelly and Harley, 2005; Kunz et al.,
328 2018; Rubatto et al., 2013; Taylor et al., 2015a, 2016, 2017).
329 Trace element data indicate that the homogeneous zircon grains/rims grew at supra-
330 solidus, and up to UHT conditions. The observed low Eu_N/Eu^* ratios (Fig. 7) generally reflects
331 zircon growth in the presence of K-feldspar produced by biotite dehydration melting reactions
332 (Rubatto et al., 2013). The >1 order of magnitude lower Nb values of homogeneous grains/rims
333 relative to zoned cores/grains (Fig. 7) is explained by the presence of rutile throughout zircon
334 crystallization, as this mineral controls most, if not all of the Nb budget of the rocks (bulk TiO_2
335 and Nb contents of ~1 wt.% and 13–18 ppm respectively are balanced by 1 wt.% rutile at
336 1400–1800 ppm Nb; see Data Table 8). This, together with quartz saturation (see
337 Supplementary Figure S3), indicates that the obtained Ti-in-zircon temperatures of 800–970
338 °C (Fig. 6) are robust (Ferry and Watson, 2007). Lastly, the high Gd_N/Yb_N and low Y–HREE
339 contents (Fig. 7) argue for zircon crystallization in the presence of garnet, which is confirmed
340 by an evaluation of zircon/garnet REE partitioning. As garnet shows homogeneous M–HREE
341 concentrations (Fig. 8a), apparent partition coefficients were calculated for each zircon
342 analysis relative to the median garnet composition. These show a good match to the
343 experimentally determined zircon/garnet partition coefficients at 900-1000 °C and 7 kbar (Fig.
344 8b), pointing to zircon growth at UHT conditions in equilibrium with garnet (Taylor et al., 2017).
345 Nevertheless, K-feldspar, rutile and garnet are stable over most of the supra-solidus
346 P–T space (see Fig. 9 and Supplementary Figure S3), which does not elucidate along which
347 portion of the P–T path the homogeneous zircon grains/rims were formed. Prograde zircon

growth has been previously proposed to form at the onset of partial melting (Hermann and Rubatto, 2003; Rubatto et al., 2013) and/or in response to the breakdown of Zr-bearing minerals (Baldwin et al., 2007; Vavra et al., 1996). However, none of these processes appears likely in our case. The minimum Ti-in-zircon temperatures (ca. 800 °C) exceed the prograde solidus by >100 °C (Fig. 9) and trace element data point to zircon growth in equilibrium with, not at the expense of other Zr-bearing minerals (rutile and garnet). Most importantly, homogeneous grains/rims show a clear trend of decreasing Ti contents with U-Pb dates, entailing continuous zircon crystallization during progressive cooling of the system, from ~940–970 °C to ~800 °C (Fig. 6). This trend is best explained by zircon formation through decreasing Zr solubility of the silicate melt along the retrograde path (Kelsey et al., 2008; Mintrone et al., 2020; Taylor et al., 2015a; Yakymchuk and Brown, 2014). This interpretation is further supported by (i) a rough increase of zircon/garnet HREE partition coefficients towards younger ages (Fig. 8c), consistent with a progressive temperature decrease (Taylor et al., 2017); and (ii) limited $\varepsilon Hf_{(t)}$ scatter (~5 εHf-units) compared to the cores (>20 εHf-units) and no variation of $\varepsilon Hf_{(t)}$ with age (Fig. 6), arguing for continuous crystallization from a relatively homogeneous melt phase.

The correlations between U-Pb dates and key zircon trace element indicators make the ~50 Myr spread of U-Pb dates shown by homogeneous grains/rims between 315 and 265 Ma (Figs. 5, 6) indicative of a truly protracted period of zircon crystallization. Analytical artifacts, such as ablation craters mixing cores and rims, can be ruled out as multiple analyses in single domains show identical dates (Fig. 4) and mixing trends between cores and rims are absent from the data (Figs. 6, 7). The low α-doses and Ti-in-zircon temperatures below their specific closure temperatures (Supplementary Figures S8 and S9) make post-crystallization disturbance of the U-Pb system equally unlikely. Therefore, we collectively interpret the zircon trace element and U-Pb data to reflect continuous, supra-solidus cooling from the thermal peak at UHT conditions (940–970 °C, highest-temperature zircons; Fig. 6) down to the solidus (~800 °C; lowest-temperature zircons).

5.1.2. Mafic granulite

The dominant population of dates from homogeneous rims/grains at 284.7 ± 2.7 Ma in sample HS15-BOU07 (Fig. 5 and Supplementary Figure S6) could be interpreted as reflecting either crystallization of a mafic magma or metamorphism of a pre-existing crustal rock, as is

generally the case in mafic granulites (e.g. Moyen et al., 2017b). In fact, the Bournac mafic granulites were originally interpreted as metamorphosed, pre-Variscan mafic rocks (Dostal et al., 1980) but subsequent zircon U-Pb dating led most authors to conclude that they represent underplated, Permian mafic magmas (Costa and Rey, 1995; Féménias et al., 2003, Rossi et al., 2006). The latter interpretation would be apparently consistent with widespread Permian magmatism recorded throughout the Variscan Belt (Boscaini et al., 2020), notably the ~283 Ma Mafic Complex of the Ivrea-Verbano Zone in NW Italy (Karakas et al., 2019). However, the trace element composition of homogeneous rims/grains in HS15-BOU07 is distinct from that of typical igneous zircon and plots off the magma differentiation trend defined by the Ivrea-Verbano zircons (Fig. 7). In particular, Permian zircons in HS15-BOU07 are richer in Ti (25–40 ppm) than magmatic zircons from the Mafic Complex of the Ivrea-Verbano Zone (5–30 ppm) (Fig. 6), pointing to different environments and/or conditions of zircon formation.

Furthermore, if the rock derives from a Permian mafic magma, the zoned zircon cores with older U-Pb dates and distinct trace element compositions must be interpreted as incompletely dissolved xenocrysts. Such xenocrysts would show a random sampling of compositionally diverse zircons from the country rocks, comparable to zoned cores/grains from the felsic granulites. In contrast, the zircon cores from HS15-BOU07 define a single trend of closed-system $^{176}Hf/^{177}Hf$ radiogenic ingrowth (Fig. 6a) and a tight compositional cluster in terms of trace element concentrations (Fig. 7). Hence, these cores likely represent a coherent, single zircon population crystallized at the same time, whose present-day range in U-Pb dates only results from variable extent of Pb loss (Laurent and Zeh, 2015).

Therefore, we interpret zoned cores from HS15-BOU07 as reflecting former igneous zircon crystallized from the protolith, whereas the homogeneous rims/grains correspond to Variscan metamorphic zircon. The Ordovician age of the oldest zircon core (481 ± 8 Ma) thereby places a minimum age for the mafic protolith. Following Dostal et al. (1980), the mafic granulite would thus correspond to a pre-Variscan, meta-igneous rock that underwent the same UHT metamorphic and partial melting history as the meta-sedimentary granulites. The homogeneous grains/rims in HS15-BOU07 likely formed through the same process as in the felsic granulites, i.e. crystallization from a cooling melt. This is supported by their homogeneous trace element compositions and εHf (Figs. 6a, 7) and overlap with homogeneous zircon rims/grains from felsic granulites in the Ti vs. U-Pb date plot (Fig. 6b). Although the mafic granulite contains neither quartz, nor rutile, the Ti-in-zircon temperatures

412 are probably not significantly different from those obtained from the felsic granulites at given
413 Ti content (using a_{SiO2} = 0.9 and a_{TiO2} = 0.7 would shift temperature up by 25 °C, which roughly
414 corresponds to the uncertainty). In this case, the shorter range of U-Pb dates in the mafic
415 granulite may reflect the lower Zr content of the sample (124 ppm) compared to felsic granulites
416 (222–234 ppm), which would have the effect of delaying zircon saturation along the cooling
417 path (Kelsey et al., 2008; Mintrone et al., 2020).
418
419 *5.2. Melt production and loss during Variscan UHT metamorphism*
420
421 Our new data demonstrate that the investigated granulites represent pre-Variscan
422 metasedimentary and meta-igneous mafic rocks metamorphosed at UHT conditions during the
423 late Variscan orogeny. Mineralogy (Fig. 2) and whole-rock compositions (Fig. 3) indicate that
424 the rocks must have lost melt to preserve anhydrous mineral assemblages, which is generally
425 considered to happen along the prograde branch of the P–T path (Brown, 2013; Kelsey and
426 Hand, 2015; White and Powell, 2002; Yakymchuk and Brown, 2014a). However, the
427 homogeneous zircon rims/grains in all samples must have formed through melt saturation
428 upon cooling from the thermal peak to the solidus (see section 5.1), meaning that at least some
429 melt was present along the retrograde path.
430 To estimate the amount of melt required to explain the crystallization of homogeneous
431 zircon rims/grains, we have applied the melt-o-meter method of Mintrone et al. (2020). This
432 method uses the Zr mass balance between the bulk sample composition, the relative
433 proportion of zircon newly crystallized from melt and the theoretical Zr solubility of such melt
434 at inferred peak temperatures (from the model of Boehnke et al., 2013), i.e. 940–970 °C here
435 (see Supplementary Material for details). The method does not intend to precisely quantify the
436 melt fraction but only give a first-order estimate to be compared to theoretical melt
437 productivities at peak conditions. The calculated fractions of newly precipitated zircon (FPZ)
438 are 67 and 83 wt.% for HS15-BOU01 and HS15-BOU17 respectively, which corresponds to
439 11–13 wt.% (ca. 15 vol.%) melt. For the mafic granulite, the calculated FPZ is 97 wt.%, which
440 yields ca. 7 wt.% (ca. 10 vol.%) melt at 940–970 °C. For the two felsic granulite samples,
441 pseudosections calculated with bulk compositions adjusted to fit the predicted peak melt
442 volume fractions (details on the melt reintegration procedure are in the Supplementary
443 Material) predict a near-solidus (810–840 °C) field characterized by decreasing garnet mode,

breaking down to biotite (Fig. 9). This reaction is not observed in the samples and would contradict zircon/garnet REE partitioning (Fig. 8), which indicates garnet stability throughout the range of zircon crystallization temperatures. Therefore, retrograde melt loss must have taken place at temperatures only slightly above 840 °C, preventing hydration of the peak mineral assemblage yet allowing for zircon crystallization from the melt phase upon cooling.

The calculated peak melt proportions (10–15 vol.%) are lower than theoretical maximum melt productivities at 5–10 kbar and 940–970 °C (30–60 vol.% and 20–40 vol.% for meta-sedimentary vs. mafic rocks, respectively; Palin et al., 2016; Webb et al., 2015 and references therein). This confirms that the E-FMC granulites have also lost substantial amounts of melt along the prograde path. Melt reintegration calculations indicate that up to 18 to 24 vol.% melt would have been lost along the prograde path for HS15-BOU01 and HS15-BOU17, respectively. This also explains the preservation of protolith zircon despite reaching UHT conditions, as prograde melt loss tends to shift up-temperature the dissolved zircon fraction isopleths (Kelsey et al., 2008; Yakymchuk and Brown, 2014b). Melt-reintegrated compositions also highlight the prograde growth of garnet as a peritectic phase (Fig. 9). Zircon thus begins to form at peak temperature in the presence of both garnet and residual melt, explaining the well-equilibrated zircon/garnet REE patterns (Fig. 8).

In summary, we propose that the Variscan P–T metamorphic history of the Bournac granulites involves: (i) prograde heating and partial melting from the solidus up to 940–970 °C (at 8 ± 2 kbar) with concomitant dissolution of protolith zircon, together with garnet growth and melt drainage reaching a cumulative loss of minimum 18–24 vol.% melt in the felsic granulites; followed by (ii) cooling with <15 vol.% residual melt and zircon crystallization, with garnet remaining stable owing to at least one last melt drainage event close to ca. 840 °C in the felsic granulites.

5.3. Timescales of melt production, extraction and crystallization in the crust

Data from our granulite xenoliths record prograde melt production and loss, followed by cooling associated with zircon crystallization and limited further melt drainage. Although other lower crustal regions might have recorded more complex histories of melt residence and transfer, the clear timing of zircon crystallization relative to the simple sequence recorded in our samples allows to temporally benchmark the thermal evolution of the lower crust and

intracrustal differentiation (Fig. 10). Indeed, based on these interpretations, the oldest homogeneous zircon rims/grains analyses from meta-sedimentary granulites should provide a minimum age for the Variscan lower crustal thermal peak in the E-FMC. The ages obtained from analyses statistically defining single populations (and comprising the spots with highest Ti-in-zircon temperatures) are 313.5 ± 3.6 Ma (MSWD = 1.8; n = 9) for HS15-BOU01 and 312.8 ± 3.1 Ma (MSWD = 1.5; n = 27) for HS15-BOU17 (Fig. 10a).

The co-genetic nature of peraluminous granites from the EFMC with the investigated felsic granulites has been established by phase equilibria modelling (Villaros et al., 2018), which is confirmed by the overlapping zircon $\varepsilon Hf_{(t)}$ between granites and granulites (Fig. 6a). The latter show on average more negative $\varepsilon Hf_{(t)}$, but this is expected whenever zircon remains a residual phase (Laurent and Zeh, 2015). Based on the theory of melt loss in migmatites, the granites should have formed prior to or synchronously with the lower crustal thermal peak (Rosenberg and Handy, 2005; White and Powell, 2002; Yakymchuk and Brown, 2014a). This is confirmed by the distribution of zircon and monazite U-Pb ages from granites within an area of ~50 km radius centered on the Bournac pipe (Fig. 10b). The number of U-Pb dates indeed increases progressively from 340 to 310 Ma, reflecting increasing melt loss along the lower crustal prograde path, with a maximum at 320-310 Ma that strikingly coincides with the inferred 313 ± 3 Ma age for the thermal peak (Fig. 10b). This is clear evidence for direct genetic and temporal links between lower crustal granulites and upper crustal granites within the framework of the melt loss theory.

In contrast, the mid-crustal Velay diatexites and granites show a highest density of U-Pb ages at 310-300 Ma, interpreted as reflecting their crystallization some 5–10 Ma after the lower crustal thermal peak (Fig. 10b). Numerical models considering the fundamental role played by melt transfer on the thermal structure of the orogenic crust predict that peak temperature conditions should be attained synchronously in the lower and the middle crust (Depine et al., 2008). Following this, it can be inferred that the Velay magmas (of mixed lower and middle crustal origin) were formed/accumulated at the latest by 313 ± 3 Ma. Their delayed crystallization would thus indicate the prevalence of a partially molten mid-crustal layer for several Myr (Vanderhaeghe et al., 2020), in contrast to the faster cooling and crystallization of granitic plutons at higher structural levels. Additionally, melts extracted along the lower crust retrograde path possibly fed the mid-crustal partially molten layer. These melts could also have

507 formed the small-volume silicic volcanic rocks/tuffs exposed throughout the EFMC in early
508 Permian (299–283 Ma), post-orogenic sedimentary basins (Michel et al., 2015).
509 The time lag between the crystallization of the oldest upper crustal granites (ca. 340
510 Ma) and the thermal peak (ca. 313 Ma) constrains the duration of suprasolidus heating in the
511 lower crust (700–970 °C) to a maximum of ca. 27 Myr (Fig. 9), from which a minimum heating
512 rate of 10 °C/Myr can be deduced. Lithospheric mantle delamination has been proposed as a
513 heat source for Variscan (U)HT metamorphism in the eastern FMC (Laurent et al., 2017;
514 Vanderhaeghe et al., 2020). Thermal models show that at reasonable mantle heat fluxes (<50
515 mW m^{-2}), the resulting abrupt temperature increase at the Moho would entail crustal melting
516 and melt-assisted heat advection upwards in the crust for 25–30 Myr until a steady-state
517 geotherm is reached (Depine et al., 2008), in excellent agreement with our timing constraints.
518 Conversely, lower crustal cooling from peak down to ca. 800°C is reflected by protracted zircon
519 crystallization between 315 and 265 Ma (Fig. 10b), corresponding to a slower cooling rate of
520 3.0 ± 1.5 °C/Myr (Fig. 6b), similar to estimates obtained from other granulite terranes (e.g.
521 Guergouz et al., 2018; Harley and Black, 1987; Harley, 1989; Kelsey et al., 2008; Mezger et
522 al., 1993). Such slow cooling rate is consistent with the long-lived presence of melt in the lower
523 crust. Indeed, melt crystallization releases latent heat and promotes lateral flow of the
524 weakened lower crust, which hinders cooling associated with tectonic exhumation
525 (Vanderhaeghe et al., 2020).
526
527 **6. Conclusions and implications**
528
529 Granulite xenoliths sampled by the Miocene Bournac pipe in the eastern FMC
530 represent pre-Variscan lower crustal rocks that underwent the same Variscan UHT
531 metamorphic episode. Partial melting started at ~340 Ma in response to lithospheric mantle
532 delamination and was followed by heating up to peak temperatures of 940-970 °C (at 6-10
533 kbar) reached at 313 ± 3 Ma. Significant melt loss throughout the prograde path and at peak
534 temperature contributed to form voluminous, 340-310 Ma upper crustal peraluminous granite
535 plutons and mid-crustal diatexites. However, the lower crust was not completely melt-depleted
536 at peak conditions, as the cooling (hence Zr saturation) of residual melt (~15 vol.%) is required
537 to explain zircon formation, in particular the trend of decreasing Ti content throughout the ~50
538 Myr period of zircon crystallization in felsic granulites. Most of the melt left in the system was

eventually drained along this retrograde path before reaching temperatures of ~840 °C (at ~280 Ma), allowing the preservation of dry assemblages in the lower crust and explaining minor volumes of late granites/rhyolites in the upper crust.

These results have important implications for the interpretation of U-Pb dates in UHT granulites and the link between granulites and granites in orogenic systems:

- Although most of the melt loss from the lower crust happens along the prograde path, some UHT granulites may not be melt-free at peak conditions and non-negligible melt loss can also take place along the retrograde path, accounting for the generally slow cooling rates observed in these settings.
- In addition to the duration spent above a certain temperature (Harley, 2016), the zircon crystallization time span in these UHT granulites also depends on the amount of melt still present at peak conditions and the Zr budget of the partly molten system, as melt cooling and saturation is the dominant zircon-forming reaction in this case.
- As a corollary, sharp peak of zircon dates in mafic granulites may me mistaken as an igneous crystallization age, whereas it rather reflects late zircon saturation closer to the solidus due to lower Zr contents than in meta-sedimentary granulites.
- The relative timing of zircon crystallization in co-genetic upper crustal granites and lower crustal granulites is a key information to understand the processes by which they are linked. In particular, prograde/peak melt loss from the lower crust to form upper crustal granites, followed by zircon saturation in granulites upon retrograde cooling, is expected to decouple U-Pb crystallization ages between the upper and lower crust, as observed here.

Acknowledgements

We thank M. Charlet, C. Doucet and A. Didier for help during fieldwork and sampling; as well as B. Devouard, G. Estrade, J.-M. Hénot, C. Guilbaud, M. Guillong, M. Leisen, C. Merlet, and B. Suchéras-Marx for assistance with sample preparation and analyses. P. Bouilhol, F. Faure, V. Gardien, J.-F. Moyen and O. Vanderhaeghe are thanked for enlightening discussions. OL and LSD thank the F.R.S.-FNRS for financial support during field campaign. SC acknowledges financial support from the “Conseil Général de l’Ardèche” while working at

ENSL. Two anonymous reviewers and the editor R. Hickey-Vargas are thanked for their very constructive and helpful comments.

Figure captions

Figure 1. (a) Sketch map depicting the exposed Variscan domains and inferred suture zones in W Europe. (b) Geological map of the eastern Massif Central and (c) interpretative cross-section, adapted from Vanderhaeghe et al. (2020). The crust and mantle structure along with approximate seismic velocities for the different layers are from Perrier and Ruegg (1973). (d) Summary of P–T estimates obtained for the three investigated crustal xenoliths; shaded areas and dotted fields represent the stability fields of mineral assemblages for our samples (derived from pseudosection analyses – see Supplementary Material) and for similar literature samples (compiled in Leyreloup, 1992), while the symbols represent average conditions of equilibration for our samples based on conventional thermobarometry.

Figure 2. Petrography of the studied granulite xenoliths. Each column shows a rock slab (scale bar is 1 cm) and optical cathodoluminescence images (scale bar is 500 µm) illustrating the mineral assemblages and the textural position of zircon grains. Abbreviations: Afs = alkali feldspar; Cpx = clinopyroxene; Grt = garnet; Ilm = ilmenite; Pl = plagioclase; Opx = orthopyroxene; Qz = quartz; Sil = sillimanite; Zrn = zircon.

Figure 3. Geochemistry of granulite xenoliths from the FMC. (a) SiO_2 vs. Al_2O_3 plot and (b) B–A cationic diagram of Villaseca et al. (1998). The dotted lines represent the contours encompassing 85% of analyses of greenschist-facies metasediments from the FMC (red; n = 80); metabasites from the high-grade allochtonous Upper Gneiss Unit (blue; n = 309); peraluminous granites from the eastern FMC (black; n = 1533). Data sources are available in the Supplementary Material. The large crossed dots depict average Ivrea stronalite compositions (from Schnetger, 1994). The melt loss vector in (b) is deduced from phase equilibria modelling of Villaros et al. (2018). (c) Ternary La–Nb–Y diagram of Cabanis and Lecolle (1989) (for mafic rocks only); (d) multi-element diagram normalized to the bulk continental crust composition of Rudnick and Gao (2014). The pink field shows the variability of the Ivrea stronalites (Schnetger, 1994).

Figure 4. Representative cathodoluminescence images of zircon grains from the granulite xenoliths investigated in this study. The white and yellow dotted circles represent the position of the laser spots for U–Pb dating/trace element (TE) and Lu–Hf isotopic analyses respectively, with corresponding spot name (S1-XX, M1-XX, M2-XX), $^{238}U/^{206}Pb$ date ±2σ uncertainty (in Ma), Ti content (in blue), and $\varepsilon Hf_{(t)}$ ± 2σ uncertainty (calculated using the $^{238}U/^{206}Pb$ date obtained on the same domain). The value with an asterisk corresponds to the $^{207}Pb/^{206}Pb$ date as the analysis was discordant.

Figure 5. Results of zircon U-Pb analyses for the Bournac granulite xenoliths shown as Tera–Wasserburg diagrams ($^{238}U/^{206}Pb$ vs. $^{207}Pb/^{206}Pb$) with error ellipses quoted at the 95% confidence level. The insets selectively represent data from homogeneous grains and rims with ellipses color-coded based on Ti contents from the same ablated volume.

Figure 6. Plots of zircon $\varepsilon Hf_{(t)}$ (a) and Ti contents (b) vs. $^{238}U/^{206}Pb$ date (considering only concordant data) for the Bournac granulite xenoliths, with a close-up focus on the Variscan period (240–340 Ma) on the left-hand side diagrams. Note the scale change at 500 Ma in the right-hand side diagrams. The Ti-in-zircon temperatures were calculated using the calibration of Ferry and Watson (2007) with $a(TiO_2) = a(SiO_2) = 1$. The grey and orange fields represent zircon data respectively from the lower crustal Mafic Complex of the Ivrea-Verbano Zone, NW Italy (Karakas et al., 2019; Storck et al., 2021) and granites from the E-FMC (Moyen et al., 2017b, with estimated zircon Ti contents based on magma temperatures proposed by Laurent et al., 2017). In (a) the orange arrow represents the isotopic evolution of bulk crust with a $^{176}Lu/^{177}Hf$ ratio of 0.015 (yellow); and the green arrows are Pb loss trends for zircon cores and homogeneous grains/rims from HS15-BOU07 using the average $^{176}Lu/^{177}Hf$ of each group. Crosses labelled “2 SE” correspond to the typical 2σ uncertainties.

Figure 7. Selected trace element plots comparing the compositions of zircons from the Bournac granulite xenoliths to those of zircon from various parental magmas and geodynamic environments (as compiled in Laurent et al., 2022), (U)HT migmatites and granulites (Kelly and Harley, 2005; Kunz et al., 2018; Rubatto et al., 2013; Taylor et al., 2015a) and the Ivrea Mafic

633 Complex (Karakas et al., 2019). For the latter, the arrows depicts the igneous evolution from
634 the most mafic to the most evolved magmas.
635
636 **Figure 8.** Evaluation of zircon/garnet REE partitioning for the felsic granulites. (a) REE
637 concentrations of zircon (Zrn) and garnet (Grt) normalized to C1 chondrite composition of
638 McDonough and Sun (1995). (b) 'Array plot' of Taylor et al. (2017) where $D_i^{zrn/grt}$ represents
639 the zircon/garnet partition coefficient of element or ratio *i* for each zircon analysis, calculated
640 using the median garnet composition of the sample. Stars represent experimental data from
641 Taylor et al. (2015b) at 7 kbar and Rubatto and Hermann (2007) at 20 kbar. (c) Plot of log
642 $D_{Yb}^{zrn/grt}$ vs. $^{206}Pb/^{238}U$ date for each zircon analysis.
643
644 **Figure 9.** Simplified P–T pseudosections calculated for the estimated subsolidus (left panels)
645 and peak (right panels) compositions of felsic granulites HS15-BOU01 and HS15-BOU17,
646 contoured for garnet mode and where major mineral reactions are indicated. The colored
647 frames depict the P-T field where the mineral assemblages of the samples are stable. The
648 inferred P–T path involves (1.) prograde heating and partial melting with concomitant melt
649 drainage (white dots), up to (2.) peak conditions of 940–970 °C (at 8 ± 2 kbar), followed by (3.)
650 cooling with ≤15 vol.% residual melt with at least one last melt drainage event (black dot) at
651 ≥840 °C. Further details on the melt reintegration procedure are provided in the Supplementary
652 Material.
653
654 **Figure 10.** Temporal relationships between granulite-facies metamorphism and granite
655 magmatism in the eastern FMC. (a) Tera-Wasserburg Concordia diagrams for the
656 homogeneous zircon rims/grains in the Bournac felsic granulites, with calculated Concordia
657 ages from the oldest population as estimates of the age of the thermal peak. (b) Schematic
658 crustal column of the eastern FMC along with the histograms and density distributions of zircon
659 and monazite U-Pb dates obtained from upper crustal granite plutons/dykes, the Velay
660 diatexite/granites (data from Chelle-Michou et al., 2017; Couzinié et al., 2014; Didier et al.,
661 2013; Laurent et al., 2017) and lower crustal metasedimentary granulites (this study). The
662 maximum at 320-310 Ma in the upper crustal rocks coincides with the inferred 313 ± 3 Ma age
663 for the lower crustal thermal peak and reflect the paroxysm of melt production and extraction

664 in the orogenic crust. In contrast, the highest density of U-Pb ages at 310-300 Ma in the Velay
665 diatexite/granites point to a delayed crystallization and is consistent with the prevalence of
666 supra-solidus conditions in the mid-crust 5–10 Ma after the thermal peak. The scattered, even
667 younger U–Pb dates in metasedimentary granulites is interpreted as reflecting protracted
668 zircon crystallization in residual lower crustal melts upon slower cooling from peak temperature
669 down to ~800°C.

670

671 **References**

672 Barbey, P., Marignac, C., Montel, J.M., Macaudière, J., Gasquet, D., Jabbori, J., 1999.
673 Cordierite growth textures and the conditions of genesis and emplacement of crustal granitic
674 magmas: the Velay Granite Complex (Massif Central, France). Journal of Petrology 40, 1423–
675 1441.

676

677 Boehnke, P., Watson, E.B., Trail, D., Harrison, T.M., Schmitt, A.K., 2013. Zircon saturation re-
678 revisited. Chemical Geology 351, 324–334. https://doi.org/10.1016/j.chemgeo.2013.05.028

679

680 Boscaini, A., Marzoli, A., Davies, J.F.H.L., Chiaradia, M., Bertrand, H., Zanetti, A., Visonà, D.,
681 De Min, A., Jourdan, F., 2020. Permian post-collisional basic magmatism from Corsica to the
682 Southeastern Alps. Lithos 376–377, 105733. https://doi.org/10.1016/j.lithos.2020.105733

683

684 Brown, M., 2013. Granite: From genesis to emplacement. Geological Society of America
685 Bulletin 125, 1079–1113. https://doi.org/10.1130/b30877.1

686

687 Cabanis, B., Lecolle, M., 1989. The La/10-Y/15-Nb/8 diagram: a tool for discrimination volcanic
688 series and evidencing continental crust magmatic mixtures and/or contamination. Comptes
689 Rendus de l'Académie des Sciences 309, 2023–2029.

690

691 Cawood, P.A., Hawkesworth, C.J., Dhuime, B., 2013. The continental record and the
692 generation of continental crust. Geological Society of America Bulletin 125, 14–32.
693 https://doi.org/10.1130/b30722.1

694

Cesare, B., Ferrero, S., Salvioli-Mariani, E., Pedron, D., Cavallo, A., 2009. “Nanogranite” and glassy inclusions: The anatectic melt in migmatites and granulites. Geology 37, 627–630. https://doi.org/10.1130/g25759a.1

Chelle-Michou, C., Laurent, O., Moyen, J.-F., Block, S., Paquette, J.-L., Couzinié, S., Gardien, V., Vanderhaeghe, O., Villaros, A., Zeh, A., 2017. Pre-Cadomian to late-Variscan odyssey of the eastern Massif Central, France: Formation of the West European crust in a nutshell. Gondwana Research 46, 170–190. https://doi.org/10.1016/j.gr.2017.02.010

Clemens, J.D., 1990. The granulite - granite connexion, in: Vielzeuf, D., Vidal, P. (Eds.), Granulites and Crustal Evolution. Kluwer, Dordrecht, pp. 25–36.

Clemens, J.D., Stevens, G., Bryan, S.E., 2020. Conditions during the formation of granitic magmas by crustal melting – Hot or cold; drenched, damp or dry? Earth-Science Reviews 200, 102982. https://doi.org/10.1016/j.earscirev.2019.102982

Collins, W.J., Murphy, J.B., Johnson, T.E., Huang, H.-Q., 2020. Critical role of water in the formation of continental crust. Nat. Geosci. 13, 331–338. https://doi.org/10.1038/s41561-020-0573-6

Connolly, J.A.D., 2009. The geodynamic equation of state: What and how. Geochemistry, Geophysics, Geosystems 10, n/a-n/a. https://doi.org/10.1029/2009gc002540

Costa, S., Rey, P., 1995. Lower crustal rejuvenation and growth during post-thickening collapse: insights from a crustal cross section through a Variscan metamorphic core complex. Geology 23, 905–908.

Couthures, J., Ablin, D., Cornette, Y., Max, N., 1991. Step-by-step eruptive dynamism in the rift of Velay: the Bournac volcano (Mezenc massif, Massif Central, France). Comptes Rendus de l’Académie des Sciences, Paris 313, 815–821.

Couzinié, S., Bouilhol, P., Laurent, O., Marko, L., Moyen, J.-F., 2021. When zircon drowns: Elusive geochronological record of water-fluxed orthogneiss melting in the Velay dome (Massif Central, France). Lithos 384–385, 105938. https://doi.org/10.1016/j.lithos.2020.105938

Couzinié, S., Laurent, O., Chelle-Michou, C., Bouilhol, P., Paquette, J.-L., Gannoun, A.-M., Moyen, J.-F., 2019. Detrital zircon U–Pb–Hf systematics of Ediacaran metasediments from the French Massif Central: Consequences for the crustal evolution of the north Gondwana margin. Precambrian Research 324, 269–284. https://doi.org/10.1016/j.precamres.2019.01.016

Couzinié, S., Laurent, O., Poujol, M., Mintrone, M., Chelle-Michou, C., Moyen, J.-F., Bouilhol, P., Vezinet, A., Marko, L., 2017. Cadomian S-type granites as basement rocks of the Variscan belt (Massif Central, France): Implications for the crustal evolution of the north Gondwana margin. Lithos 286–287, 16–34. https://doi.org/10.1016/j.lithos.2017.06.001

Crawford, A., Falloon, T., Eggins, S., 1987. The origin of island arc high-alumina basalts. Contributions to Mineralogy and Petrology 97, 417–430. https://doi.org/10.1007/BF00372004

Depine, G.V., Andronicos, C.L., Phipps-Morgan, J., 2008. Near-isothermal conditions in the middle and lower crust induced by melt migration. Nature 452, 80–3. https://doi.org/10.1038/nature06689

Didier, A., Bosse, V., Boulvais, P., Bouloton, J., Paquette, J.L., Montel, J.M., Devidal, J.L., 2013. Disturbance versus preservation of U–Th–Pb ages in monazite during fluid–rock interaction: textural, chemical and isotopic in situ study in microgranites (Velay Dome, France). Contributions to Mineralogy and Petrology 165, 1051–1072. https://doi.org/10.1007/s00410-012-0847-0

Dostal, J., Dupuy, C., Leyreloup, A.F., 1980. Geochemistry and petrology of meta-igneous granulitic xenoliths in Neogene rocks of the Massif Central, France - Implications for the lower crust. Earth and Planetary Science Letters 50, 31–40.

Downes, H., Dupuy, C., Leyreloup, A.F., 1990. Crustal evolution of the Hercynian belt of Western Europe: Evidence from lower-crustal granulitic xenoliths (French Massif Central). Chemical Geology 83, 209–231.

Downes, H., Leyreloup, A.F., 1986. Granulitic xenoliths from the French Massif Central - petrology, Sr and Nd isotope systematics and model age estimates. Geological Society, London, Special Publications 24, 319–330.

Downes, H., Shaw, A., Williamson, B.J., Thirlwall, M.F., 1997. Sr, Nd and Pb isotopic evidence for the lower crustal origin of Hercynian granodiorites and monzogranites, Massif Central, France. Chemical Geology 136, 99–122.

Féménias, O., Coussaert, N., Bingen, B., Whitehouse, M., Mercier, J.-C.C., Demaiffe, D., 2003. A Permian underplating event in late- to post-orogenic tectonic setting. Evidence from the mafic–ultramafic layered xenoliths from Beaunit (French Massif Central). Chemical Geology 199, 293–315. https://doi.org/10.1016/s0009-2541(03)00124-4

Ferry, J.M., Watson, E.B., 2007. New thermodynamic models and revised calibrations for the Ti-in-zircon and Zr-in-rutile thermometers. Contrib Mineral Petrol 154, 429–437. https://doi.org/10.1007/s00410-007-0201-0

Gao, P., Zheng, Y., Zhao, Z., 2016. Experimental melts from crustal rocks: A lithochemical constraint on granite petrogenesis. Lithos 266–267, 133–157. https://doi.org/10.1016/j.lithos.2016.10.005

Guergouz, C., Martin, L., Vanderhaeghe, O., Thébaud, N., Fiorentini, M., 2018. Zircon and monazite petrochronologic record of prolonged amphibolite to granulite facies metamorphism in the Ivrea-Verbano and Strona-Ceneri Zones, NW Italy. Lithos 308–309, 1–18. https://doi.org/10.1016/j.lithos.2018.02.014

Hacker, B.R., Kelemen, P.B., Behn, M.D., 2015. Continental Lower Crust. Annual Review of Earth and Planetary Sciences 43, 167–205.

Harley, S.L., 1989. The origins of granulites: a metamorphic perspective. Geological Magazine 126(3), 215–247.

Harley, S.L., 2016. A matter of time: The importance of the duration of UHT metamorphism. Journal of Mineralogical and Petrological Sciences 111, 50–72. https://doi.org/10.2465/jmps.160128

Harley, S.L., and Black, L.P., 1987. The Archaean geological evolution of Enderby Land, Antarctica. In: Park ,R.G., and Tarney, J. (eds), Evolution of the Lewisian and Comparable Precambrian High Grade Terrains, Geological Society Special Publication no. 27, pp. 285–296.

Harris, N., Vance, D., Ayres, M., 2000. From sediment to granite: timescales of anatexis in the upper crust. Chemical Geology 162, 155–167. https://doi.org/10.1016/S0009-2541(99)00121-7

Hermann, J., Rubatto, D., 2003. Relating zircon and monazite domains to garnet growth zones: age and duration of granulite facies metamorphism in the Val Malenco lower crust. Journal of Metamorphic Geology 21, 833–852. https://doi.org/10.1046/j.1525-1314.2003.00484

Holdaway, M.J., 2001. Recalibration of the GASP geobarometer in light of recent garnet and plagioclase activity models and versions of the garnet-biotite geothermometer. American Mineralogist 86, 1117–1129. https://doi.org/10.2138/am-2001-1001

Jagoutz, O., Klein, B., 2018. On the importance of crystallization-differentiation for the generation of SiO2-rich melts and the compositional build-up of arc (and continental) crust. American Journal of Science 318, 29–63. https://doi.org/10.2475/01.2018.03

Karakas, O., Wotzlaw, J.-F., Guillong, M., Ulmer, P., Brack, P., Economos, R., Bergantz, G.W., Sinigoi, S., Bachmann, O., 2019. The pace of crustal-scale magma accretion and

820 differentiation beneath silicic caldera volcanoes. Geology 47, 719–723.
821 https://doi.org/10.1130/G46020.1
822
823 Kelly, N.M. and Harley, S.L., 2005. An integrated microtextural and chemical approach to
824 zircon geochronology: refining the Archaean history of the Napier Complex, east Antarctica.
825 Contributions to Mineralogy and Petrology 149, 57–84.
826
827 Kelsey, D.E., Clark, C., Hand, M., 2008. Thermobarometric modelling of zircon and monazite
828 growth in melt-bearing systems: examples using model metapelitic and metapsammitic
829 granulites. Journal of Metamorphic Geology 26, 199–212. https://doi.org/10.1111/j.1525-
830 1314.2007.00757.x
831
832 Kelsey, D.E., Hand, M., 2015. On ultrahigh temperature crustal metamorphism: Phase
833 equilibria, trace element thermometry, bulk composition, heat sources, timescales and tectonic
834 settings. Geoscience Frontiers 6, 311–356. https://doi.org/10.1016/j.gsf.2014.09.006
835
836 Kunz, B.E., Regis, D., Engi, M., 2018. Zircon ages in granulite facies rocks: decoupling from
837 geochemistry above 850° C? Contributions to Mineralogy and Petrology 173, 1–21.
838
839 Laurent, O., Couzinié, S., Zeh, A., Vanderhaeghe, O., Moyen, J.-F., Villaros, A., Gardien, V.,
840 Chelle-Michou, C., 2017. Protracted, coeval crust and mantle melting during Variscan late-
841 orogenic evolution: U–Pb dating in the eastern French Massif Central. International Journal of
842 Earth Sciences 106, 421–451. https://doi.org/10.1007/s00531-016-1434-9
843
844 Laurent, O., Moyen, J.-F., Wotzlaw, J.-F., Björnsen, J., Bachmann, O., 2021. Early Earth
845 zircons formed in residual granitic melts produced by tonalite differentiation. Geology 50, 437–
846 441. https://doi.org/10.1130/G49232.1
847
848 Laurent, O. and Zeh, A., 2015. A linear Hf isotope-age array despite different granitoid sources
849 and complex Archean geodynamics: Example from the Pietersburg block (South Africa). Earth
850 and Planetary Science Letters 430, 326–338.
851

852 Ledru, P., Courrioux, G., Dallain, C., Lardeaux, J.M., Montel, J.M., Vanderhaeghe, O., Vitel,
853 G., 2001. The Velay dome (French Massif Central): melt generation and granite emplacement
854 during orogenic evolution. Tectonophysics 342, 207–237.
855
856 Leyreloup, A.F., 1992. La croûte métamorphique du Sud de la France (Massif Central,
857 Languedoc). Géologie de surface et des enclaves remontées par les volcans cénozoïques : le
858 rôle des intrusions mafiques basicrustales dans la croûte inférieure (Thèse d'Etat). Montpellier.
859
860 Leyreloup, A.F., Dupuy, C., Andriambololona, R., 1977. Catazonal xenoliths in French
861 Neogene volcanic rocks: constitution of the Lower Crust 2. Chemical compostion and
862 consequences of the evolution of the French Massif Central Precambrian crust. Contributions
863 to Mineralogy and Petrology 67, 283–300.
864
865 McDonough, W.F. and Sun, S.S., 1995. The composition of the Earth. Chemical Geology 120,
866 223–253.
867
868 Mezger, K., Essene, E.J., van der Pluijm, B.A., Halliday, A.N., 1993. U-Pb geochronology of
869 the Grenville Orogen of Ontario and New York: constraints on ancient crustal tectonics.
870 Contributions to Mineralogy and Petrology 114, 13–26.
871
872 Michel, L.A., Tabor, N.J., Montañez, I.P., Schmitz, M.D., Davydov, V.I., 2015.
873 Chronostratigraphy and Paleoclimatology of the Lodève Basin, France: Evidence for a pan-
874 tropical aridification event across the Carboniferous–Permian boundary. Palaeogeography,
875 Palaeoclimatology, Palaeoecology 430, 118–131.
876 https://doi.org/10.1016/j.palaeo.2015.03.020
877
878 Michon, L., Merle, O., 2001. The evolution of the Massif Central Rift; spatio-temporal
879 distribution of the volcanism. Bulletin de la Société Géologique de France 172, 201–211.
880 https://doi.org/10.2113/172.2.201
881

Mintrone, M., Galli, A., Laurent, O., Chelle-Michou, C., Schmidt, M.W., 2020. Quantifying frozen melt in crustal rocks: A new melt-o-meter based on zircon rim volumes. Chemical Geology 551, 119755. https://doi.org/10.1016/j.chemgeo.2020.119755

Montel, J.M., Marignac, C., Barbey, P., Pichavant, M., 1992. Thermobarometry and granite genesis: the Hercynian low-P, high-T Velay anatectic dome (French Massif Central). Journal of Metamorphic Geology 10, 1–15.

Moyen, J.F., Laurent, O., Chelle-Michou, C., Couzinié, S., Vanderhaeghe, O., Zeh, A., Villaros, A., Gardien, V., 2017a. Collision vs. subduction-related magmatism: Two contrasting ways of granite formation and implications for crustal growth. Lithos 277, 154–177. https://doi.org/10.1016/j.lithos.2016.09.018

Moyen, J.F., Paquette, J.L., Ionov, D.A., Gannoun, A., Korsakov, A.V., Golovin, A.V., Moine, B.N., 2017b. Paleoproterozoic rejuvenation and replacement of Archaean lithosphere: Evidence from zircon U–Pb dating and Hf isotopes in crustal xenoliths at Udachnaya, Siberian craton. Earth and Planetary Science Letters 457, 149–159. https://doi.org/10.1016/j.epsl.2016.09.046

Palin, R.M., White, R.W., Green, E.C.R., Diener, J.F.A., Powell, R., Holland, T.J.B., 2016. High-grade metamorphism and partial melting of basic and intermediate rocks. Journal of Metamorphic Geology 34, 871–892. https://doi.org/10.1111/jmg.12212

Perrier, G., Ruegg, J.-C., 1973. Structure profonde du Massif Central français. Annales géophysiques 29, 435–502.

Petford, N., Cruden, A.R., McCaffrey, K.J.W., Vigneresse, J.-L., 2000. Granite magma formation, transport and emplacement in the Earth's crust. Nature 408, 669–673. https://doi.org/10.1038/35047000

Putirka, K.D., 2008. Thermometers and Barometers for Volcanic Systems. Reviews in Mineralogy and Geochemistry 69, 61–120. https://doi.org/10.2138/rmg.2008.69.3

914

915 Rabinowicz, M., Vigneresse, J.-L., 2004. Melt segregation under compaction and shear
916 channeling: Application to granitic magma segregation in a continental crust. Journal of
917 Geophysical Research: Solid Earth 109. https://doi.org/10.1029/2002JB002372

918

919 Redler, C., White, R.W., Johnson, T.E., 2013. Migmatites in the Ivrea Zone (NW Italy):
920 Constraints on partial melting and melt loss in metasedimentary rocks from Val Strona di
921 Omegna. Lithos 175–176, 40–53. https://doi.org/10.1016/j.lithos.2013.04.019

922

923 Rosenberg, C.L., Handy, M.R., 2005. Experimental deformation of partially melted granite
924 revisited: implications for the continental crust. Journal of Metamorphic Geology 23, 19–28.
925 https://doi.org/10.1111/j.1525-1314.2005.00555.x

926

927 Rossi, P., Cocherie, A., Fanning, C.M., Deloule, E., 2006. Variscan to eo-Alpine events
928 recorded in European lower-crust zircons sampled from the French Massif Central and
929 Corsica, France. Lithos 87, 235–260. https://doi.org/10.1016/j.lithos.2005.06.009

930

931 Rubatto, D., Chakraborty, S., Dasgupta, S., 2013. Timescales of crustal melting in the Higher
932 Himalayan Crystallines (Sikkim, Eastern Himalaya) inferred from trace element-constrained
933 monazite and zircon chronology. Contributions to Mineralogy and Petrology 165, 349–372.

934

935 Rubatto, D. and Hermann, J., 2007. Experimental zircon/melt and zircon/garnet trace element
936 partitioning and implications for the geochronology of crustal rocks. Chemical Geology, 241(1–
937 2), 38–61.

938

939 Rudnick, R., Gao, S., 2014. 4.1 - Composition of the Continental Crust, in: Treatise on
940 Geochemistry. Eds.: H. D. Holland, K. K. Turekian.

941

942 Sawyer, E.W., Cesare, B., Brown, M., 2011. When the Continental Crust Melts. Elements 7,
943 229–234. https://doi.org/10.2113/gselements.7.4.229

944

945 Scaillet, B., Searle, M.P., 2006. Mechanisms and timescales of felsic magma segregation,
946 ascent and emplacement in the Himalaya. Geological Society, London, Special Publications
947 268, 293–308.
948
949 Schnetger, B., 1994. Partial melting during the evolution of the amphibolite- to granulite-facies
950 gneisses of the Ivrea Zone, northern Italy. Chemical Geology 113, 71–101.
951 https://doi.org/10.1016/0009-2541(94)90006-X
952
953 Storck, J.-C., Laurent, O., Karakas, O., Wotzlaw, J.-F., Galli, A., Sinigoi, S., Bachmann, O.,
954 Chelle-Michou, C., 2021. Mantle versus crustal contributions in crustal-scale magmatic
955 systems (Sesia Magmatic System, northern Italy) from coupling Hf isotopes and numerical
956 modelling. Contrib Mineral Petrol 176, 95. https://doi.org/10.1007/s00410-021-01847-9
957
958 Taylor, R.J., Clark, C., Fitzsimons, I.C., Santosh, M., Hand, M., Evans, N., McDonald, B., 2014.
959 Post-peak, fluid-mediated modification of granulite facies zircon and monazite in the
960 Trivandrum Block, southern India. Contributions to Mineralogy and Petrology 168, 1–17.
961
962 Taylor, R.J.M., Clark, C., Harley, S.L., Kylander-Clark, A.R.C., Hacker, B.R., Kinny, P.D., 2017.
963 Interpreting granulite facies events through rare earth element partitioning arrays. Journal of
964 Metamorphic Geology 35, 759–775. https://doi.org/10.1111/jmg.12254
965
966 Taylor, R.J.M., Clark, C., Johnson, T.E., Santosh, M., Collins, A.S., 2015a. Unravelling the
967 complexities in high-grade rocks using multiple techniques – The Achankovil Zone of southern
968 India. Contributions to Mineralogy and Petrology, 169(5), 1–19.
969
970 Taylor, R.J.M., Harley, S.L., Hinton, R.W., Elphick, S., Clark, C., Kelly, N.M., 2015b.
971 Experimental determination of REE partition coefficients between zircon, garnet and melt: A
972 key to understanding high-T crustal processes. Journal of Metamorphic Geology 33(3), 231–
973 248.
974

975 Taylor, R.J.M., Kirkland, C.L., Clark, C., 2016. Accessories after the facts: Constraining the
976 timing, duration and conditions of high-temperature metamorphic processes. Lithos 264, 239–
977 257. https://doi.org/10.1016/j.lithos.2016.09.004
978
979 Vanderhaeghe, O., Laurent, O., Gardien, V., Moyen, J.-F., Gébelin, A., Chelle-Michou, C.,
980 Couzinié, S., Villaros, A., Bellanger, M., 2020. Flow of partially molten crust controlling
981 construction, growth and collapse of the Variscan orogenic belt: the geologic record of the
982 French Massif Central. BSGF. https://doi.org/10.1051/bsgf/2020013
983
984 Vavra, G., Gebauer, D., Schmid, R., Compston, W., 1996. Multiple zircon growth and
985 recrystallization during polyphase Late Carboniferous to Triassic metamorphism in granulites
986 of the Ivrea Zone (Southern Alps): an ion microprobe (SHRIMP) study. Contrib Mineral Petrol
987 122, 337–358. https://doi.org/10.1007/s004100050132
988
989 Vielzeuf, D., Clemens, J.D., Pin, C., Moinet, E., 1990. Granites, granulites, and crustal
990 differentiation, in: Vielzeuf, D., Vidal, P. (Eds.), Granulites and Crustal Evolution. Kluwer,
991 Dordrecht, pp. 59–85.
992
993 Villaros, A., Laurent, O., Couzinié, S., Moyen, J.-F., Mintrone, M., 2018. Plutons and domes:
994 the consequences of anatectic magma extraction—example from the southeastern French
995 Massif Central. Int J Earth Sci (Geol Rundsch) 107, 2819–2842.
996 https://doi.org/10.1007/s00531-018-1630-x
997
998 Villaseca, C., Barbero, L., Herreros, V., 1998. A re-examination of the typology of peraluminous
999 granite types in intracontinental orogenic belts. Transactions of the Royal Society of Edinburgh.
1000
1001 Webb, G., Powell, R., McLaren, S., 2015. Phase equilibria constraints on the melt fertility of
1002 crustal rocks: the effect of subsolidus water loss. Journal of Metamorphic Geology 33, 147–
1003 165. https://doi.org/10.1111/jmg.12114
1004

White, R., Powell, R., 2002. Melt loss and the preservation of granulite facies mineral assemblages. Journal of Metamorphic Geology 20, 621–632. https://doi.org/10.1046/j.1525-1314.2002.00206.x

White, R.W., Powell, R., Holland, T.J.B., 2001. Calculation of partial melting equilibria in the system Na_2O-CaO-K_2O-FeO-MgO-Al_2O_3-SiO_2-H_2O (NCKFMASH). Journal of Metamorphic Geology 19, 139–153.

Williamson, B.J., Downes, H., Thirlwall, M.F., Beard, A.D., 1997. Geochemical constraints on restite composition and unmixing in the Velay anatectic granite, French Massif Central. Lithos 40, 295–319.

Yakymchuk, C., Brown, M., 2014a. Consequences of open-system melting in tectonics. Journal of the Geological Society 171, 21–40.

Yakymchuk, C., Brown, M., 2014b. Behaviour of zircon and monazite during crustal melting. Journal of the Geological Society 171, 465–479. https://doi.org/10.1144/jgs2013-115

Zheng, Y.-F., Gao, P., 2021. The production of granitic magmas through crustal anatexis at convergent plate boundaries. Lithos, 9th Hutton Symposium on the Origin of Granites and Related Rocks 402–403, 106232. https://doi.org/10.1016/j.lithos.2021.106232

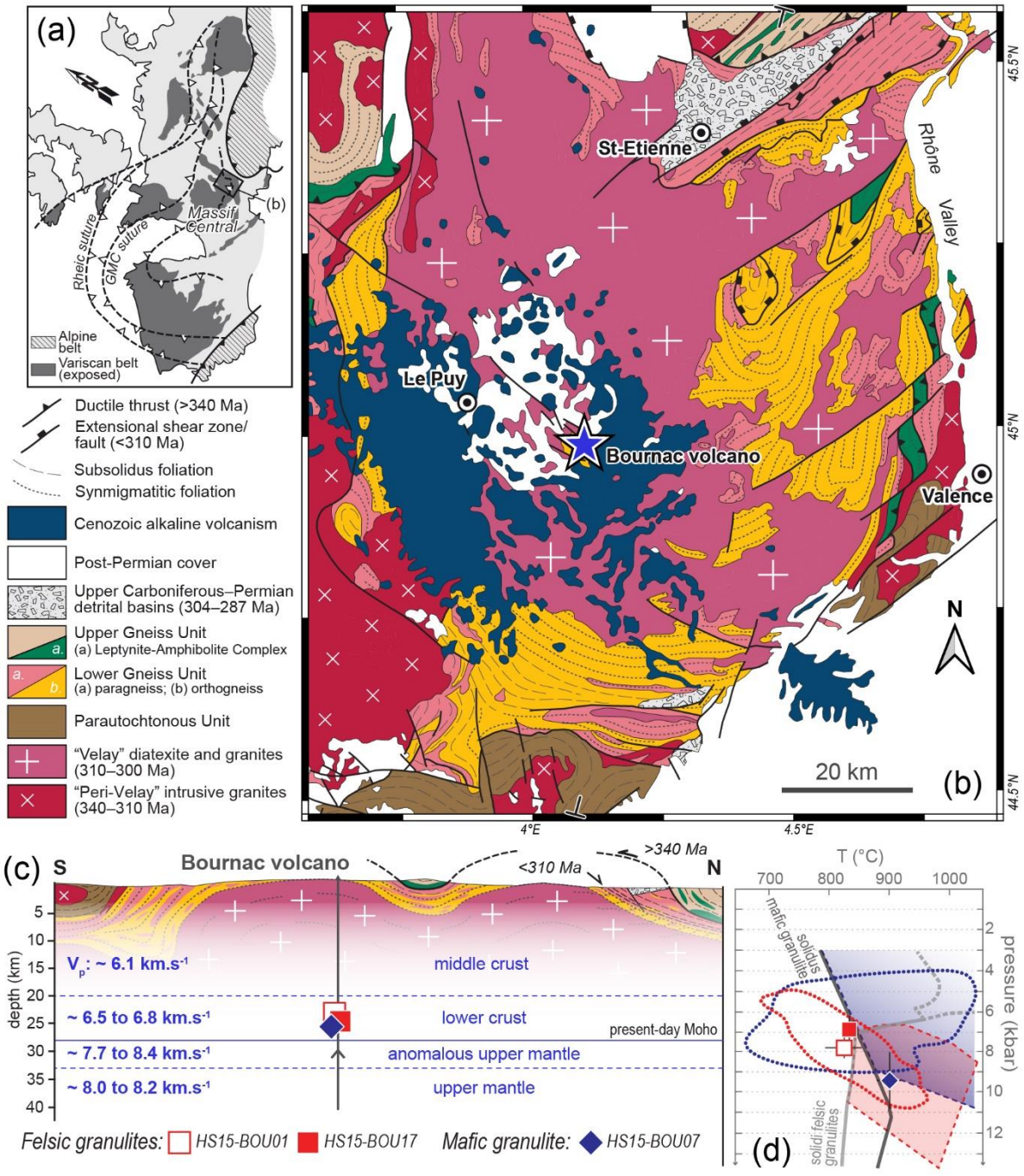
(a)
(b)
Massif Central
Rheic suture
GMC suture
Alpine belt
Variscan belt (exposed)
Ductile thrust (>340 Ma)
Extensional shear zone/ fault (<310 Ma)
Subsolidus foliation
Synmigmatitic foliation
Cenozoic alkaline volcanism
Post-Permian cover
Upper Carboniferous–Permian detrital basins (304–287 Ma)
Upper Gneiss Unit
(a) Leptynite-Amphibolite Complex
Lower Gneiss Unit
(a) paragneiss; (b) orthogneiss
Parautochtonous Unit
"Velay" diatexite and granites (310–300 Ma)
"Peri-Velay" intrusive granites (340–310 Ma)
St-Etienne
Rhône
Valley
Le Puy
Bournac volcano
Valence
N
20 km
(b)
45.5°N
45°N
44.5°N
4°E
4.5°E
(c) s
Bournac volcano
<310 Ma
>340 Ma
N
depth (km)
5
10
15
20
25
30
35
40
V_p: ~ 6.1 km.s-1
middle crust
~ 6.5 to 6.8 km.s-1
lower crust
present-day Moho
~ 7.7 to 8.4 km.s-1
anomalous upper mantle
~ 8.0 to 8.2 km.s-1
upper mantle
Felsic granulites: HS15-BOU01 HS15-BOU17
Mafic granulite: HS15-BOU07
T (°C)
700
800
900
1000
mafic granulite
solidus
solidi felsic granulites
pressure (kbar)
2
4
6
8
10
12
(d)

Figure 1

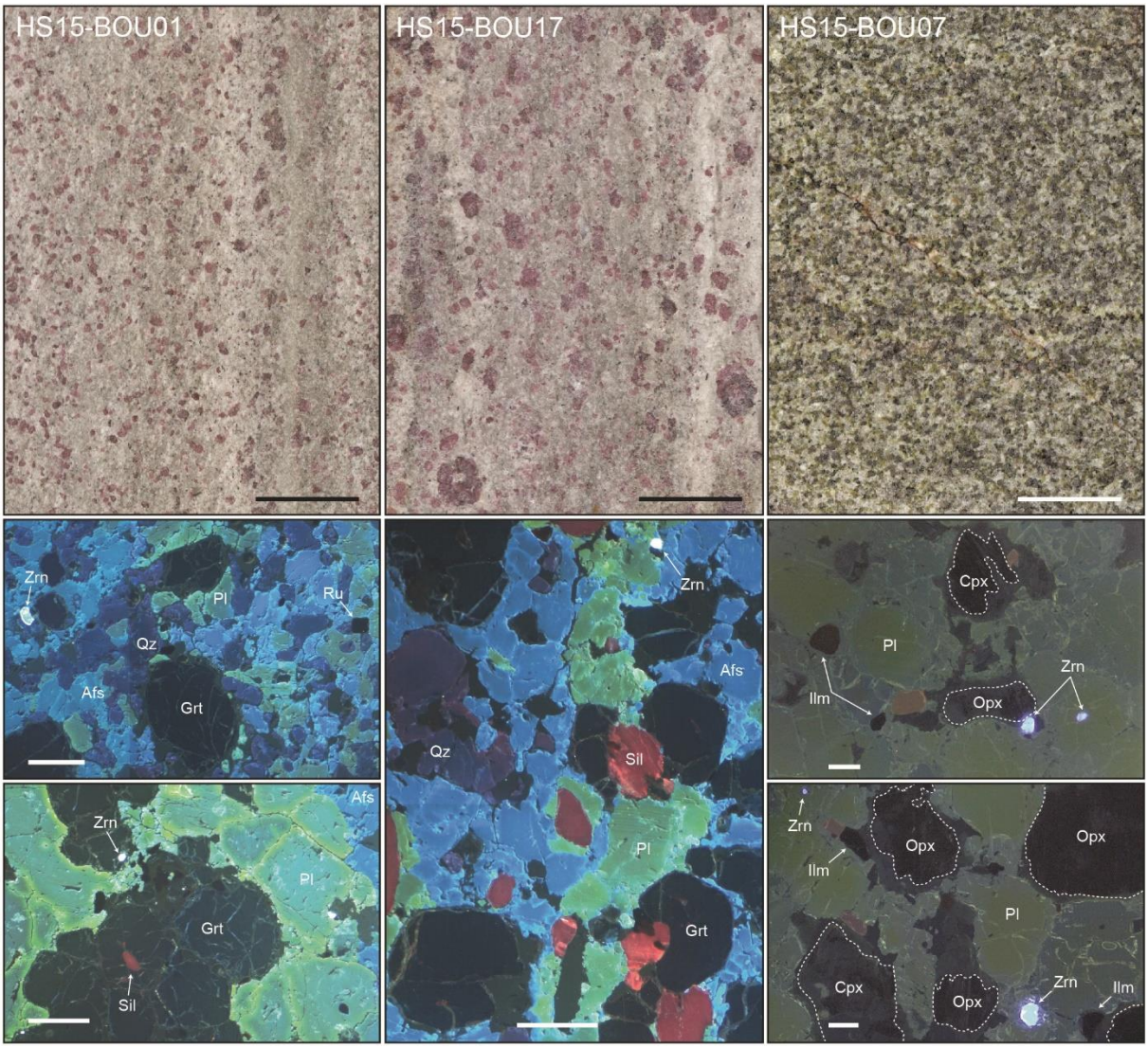
HS15-BOU01
HS15-BOU17
HS15-BOU07
Zrn
Pl
Ru
Qz
Afs
Grt
Zrn
Afs
Qz
Sil
Pl
Grt
Cpx
Pl
Zrn
Ilm
Opx
Afs
Zrn
Pl
Grt
Sil
Zrn
Opx
Opx
Ilm
Pl
Cpx
Opx
Zrn
Ilm

Figure 2

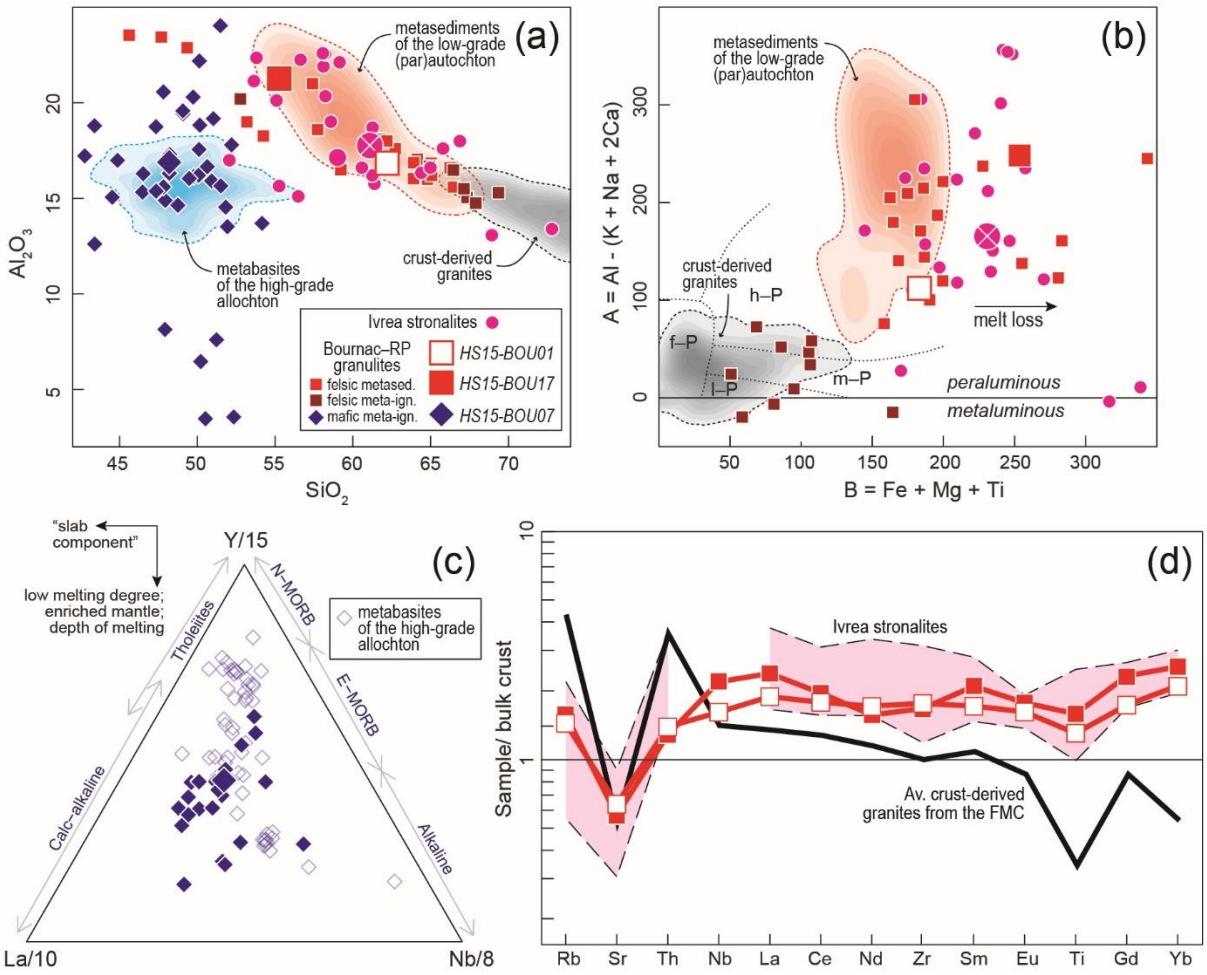
(a)
metasediments of the low-grade (par)autochton
metabasites of the high-grade allochton
crust-derived granites
Ivrea stronalites
Bournac–RP granulites
felsic metased.
felsic meta-ign.
mafic meta-ign.
HS15-BOU01
HS15-BOU17
HS15-BOU07
Al2O3
SiO2
(b)
metasediments of the low-grade (par)autochton
crust-derived granites
h–P
f–P
l–P
m–P
melt loss
peraluminous
metaluminous
A = Al - (K + Na + 2Ca)
B = Fe + Mg + Ti
(c)
"slab component"
low melting degree; enriched mantle; depth of melting
Y/15
La/10
Nb/8
Tholeiites
N-MORB
E-MORB
Alkaline
Calc-alkaline
metabasites of the high-grade allochton
(d)
Ivrea stronalites
Av. crust-derived granites from the FMC
Sample/ bulk crust
Rb
Sr
Th
Nb
La
Ce
Nd
Zr
Sm
Eu
Ti
Gd
Yb

Figure 3

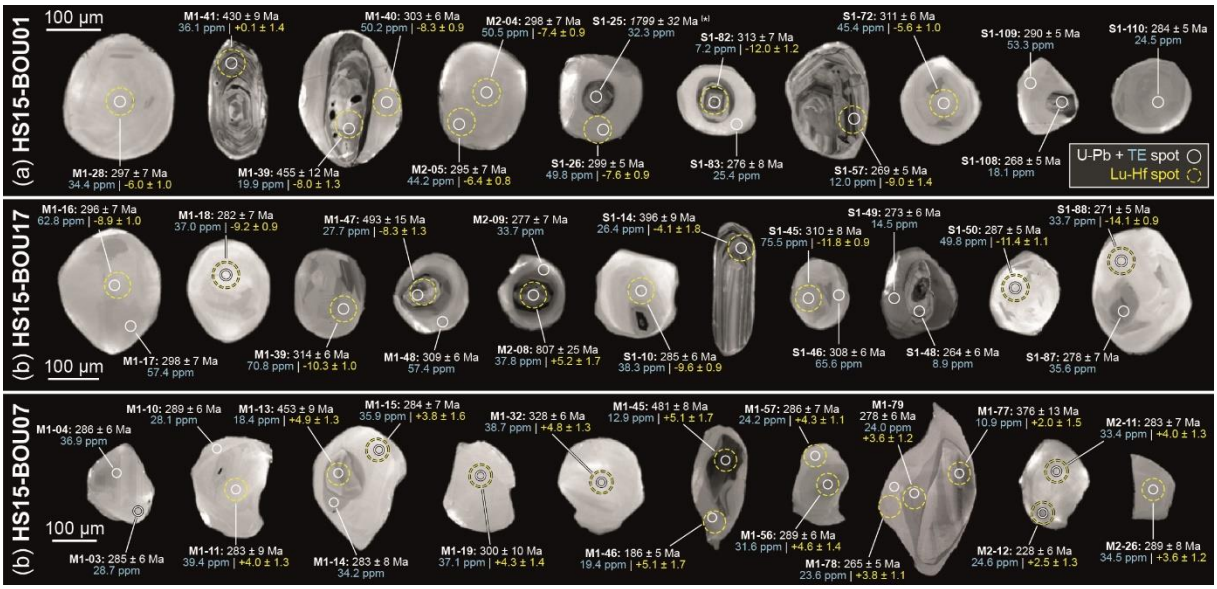
(a) HS15-BOU01
100 µm
M1-41: 430 ± 9 Ma
36.1 ppm | +0.1 ± 1.4
M1-40: 303 ± 6 Ma
50.2 ppm | -8.3 ± 0.9
M2-04: 298 ± 7 Ma
50.5 ppm | -7.4 ± 0.9
S1-25: 1799 ± 32 Ma [a]
32.3 ppm
S1-72: 311 ± 6 Ma
45.4 ppm | -5.6 ± 1.0
S1-109: 290 ± 5 Ma
53.3 ppm
S1-110: 284 ± 5 Ma
24.5 ppm
S1-82: 313 ± 7 Ma
7.2 ppm | -12.0 ± 1.2
M1-28: 297 ± 7 Ma
34.4 ppm | -6.0 ± 1.0
M1-39: 455 ± 12 Ma
19.9 ppm | -8.0 ± 1.3
M2-05: 295 ± 7 Ma
44.2 ppm | -6.4 ± 0.8
S1-26: 299 ± 5 Ma
49.8 ppm | -7.6 ± 0.9
S1-83: 276 ± 8 Ma
25.4 ppm
S1-57: 269 ± 5 Ma
12.0 ppm | -8.0 ± 1.4
S1-108: 268 ± 5 Ma
18.1 ppm
U-Pb + TE spot
Lu-Hf spot
(b) HS15-BOU17
100 µm
M1-16: 298 ± 7 Ma
62.8 ppm | -8.9 ± 1.0
M1-18: 282 ± 7 Ma
37.0 ppm | -9.2 ± 0.9
M1-47: 493 ± 15 Ma
27.7 ppm | -8.3 ± 1.3
M2-09: 277 ± 7 Ma
33.7 ppm
S1-14: 396 ± 9 Ma
26.4 ppm | -4.1 ± 1.8
S1-45: 310 ± 8 Ma
75.5 ppm | -11.8 ± 0.9
S1-49: 273 ± 6 Ma
14.5 ppm
S1-50: 287 ± 5 Ma
49.8 ppm | -11.4 ± 1.1
S1-88: 271 ± 5 Ma
33.7 ppm | -14.1 ± 0.9
M1-17: 298 ± 7 Ma
57.4 ppm
M1-39: 314 ± 6 Ma
70.8 ppm | -10.3 ± 1.0
M1-48: 309 ± 6 Ma
57.4 ppm
M2-08: 807 ± 25 Ma
37.8 ppm | +5.2 ± 1.7
S1-10: 285 ± 6 Ma
38.3 ppm | -9.6 ± 0.9
S1-46: 308 ± 6 Ma
65.6 ppm
S1-48: 264 ± 6 Ma
8.9 ppm
S1-87: 278 ± 7 Ma
35.6 ppm
(b) HS15-BOU07
100 µm
M1-04: 286 ± 6 Ma
36.9 ppm
M1-10: 289 ± 6 Ma
28.1 ppm
M1-13: 453 ± 9 Ma
18.4 ppm | +4.9 ± 1.3
M1-15: 284 ± 7 Ma
35.9 ppm | +3.8 ± 1.6
M1-32: 328 ± 6 Ma
38.7 ppm | +4.8 ± 1.3
M1-45: 481 ± 8 Ma
12.9 ppm | +5.1 ± 1.7
M1-57: 286 ± 7 Ma
24.2 ppm | +4.3 ± 1.1
M1-79
278 ± 6 Ma
24.0 ppm
+3.8 ± 1.2
M1-77: 376 ± 13 Ma
10.9 ppm | +2.0 ± 1.5
M2-11: 283 ± 7 Ma
33.4 ppm | +4.0 ± 1.3
M1-03: 285 ± 6 Ma
28.7 ppm
M1-11: 283 ± 9 Ma
39.4 ppm | +4.0 ± 1.3
M1-14: 283 ± 8 Ma
34.2 ppm
M1-19: 300 ± 10 Ma
37.1 ppm | +4.3 ± 1.4
M1-46: 186 ± 5 Ma
19.4 ppm | +5.1 ± 1.7
M1-56: 289 ± 6 Ma
31.6 ppm | +4.6 ± 1.4
M1-78: 265 ± 5 Ma
23.6 ppm | +3.8 ± 1.1
M2-12: 228 ± 6 Ma
24.6 ppm | +2.5 ± 1.3
M2-26: 289 ± 8 Ma
34.5 ppm | +3.6 ± 1.2

Figure 4

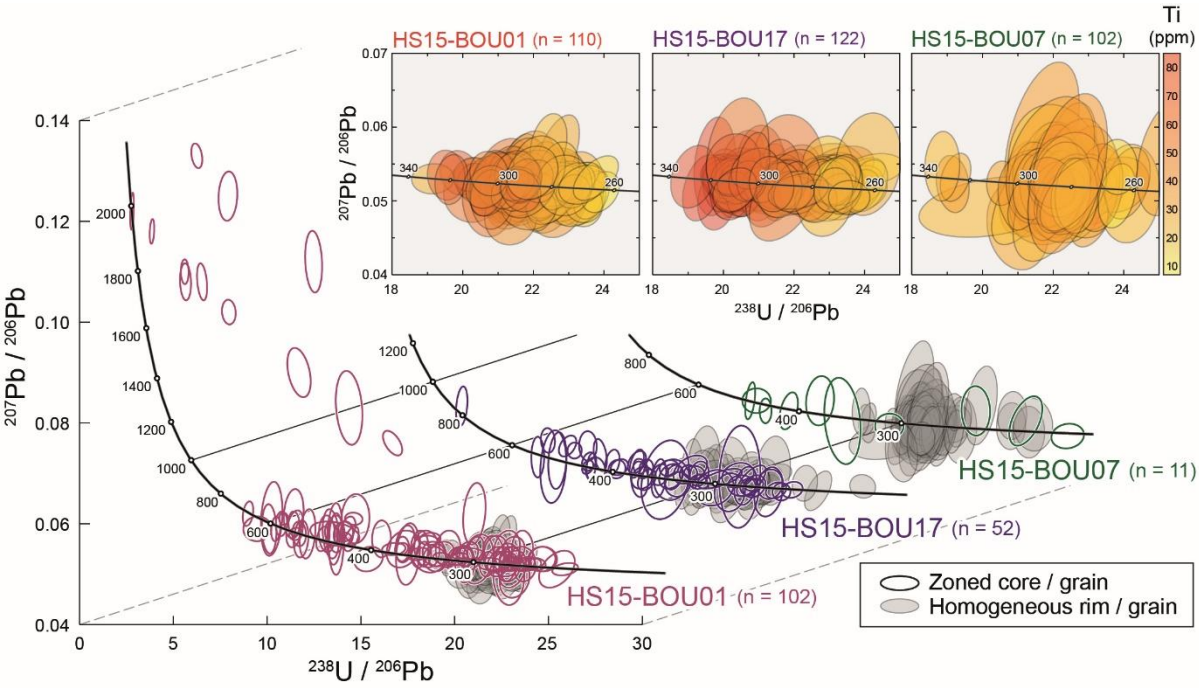
HS15-BOU01 (n = 110)
HS15-BOU17 (n = 122)
HS15-BOU07 (n = 102)
Ti (ppm)
^{207}Pb / ^{206}Pb
^{238}U / ^{206}Pb
HS15-BOU07 (n = 11)
HS15-BOU17 (n = 52)
HS15-BOU01 (n = 102)
Zoned core / grain
Homogeneous rim / grain

Figure 5

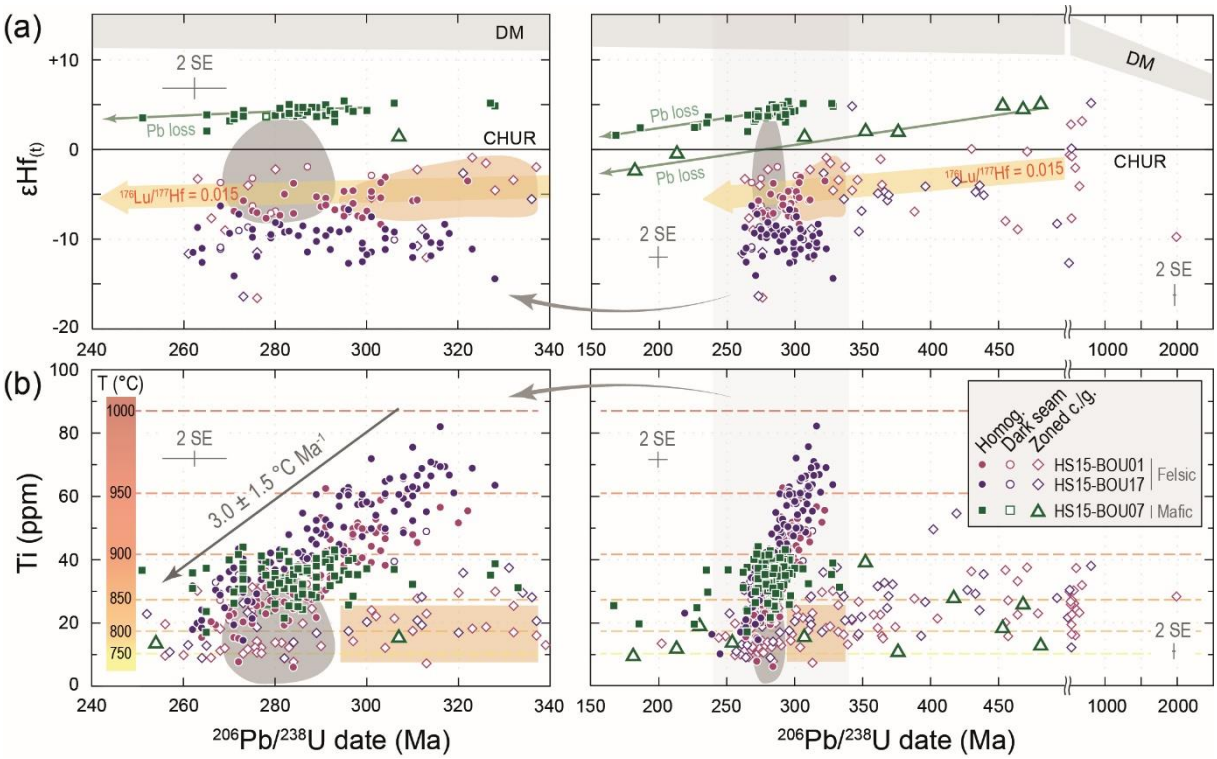
(a)
DM
+10
2 SE
Pb loss
CHUR
εHf(t)
0
-10
-20
176Lu/177Hf = 0.015
240
260
280
300
320
340
150
200
250
300
350
400
450
1000
2000
(b)
T (°C)
1000
950
900
850
800
750
100
80
60
40
20
0
Ti (ppm)
3.0 ± 1.5 °C Ma-1
Homog.
Dark seam
Zoned c./g.
HS15-BOU01
HS15-BOU17
Felsic
HS15-BOU07
Mafic
206Pb/238U date (Ma)

Figure 6

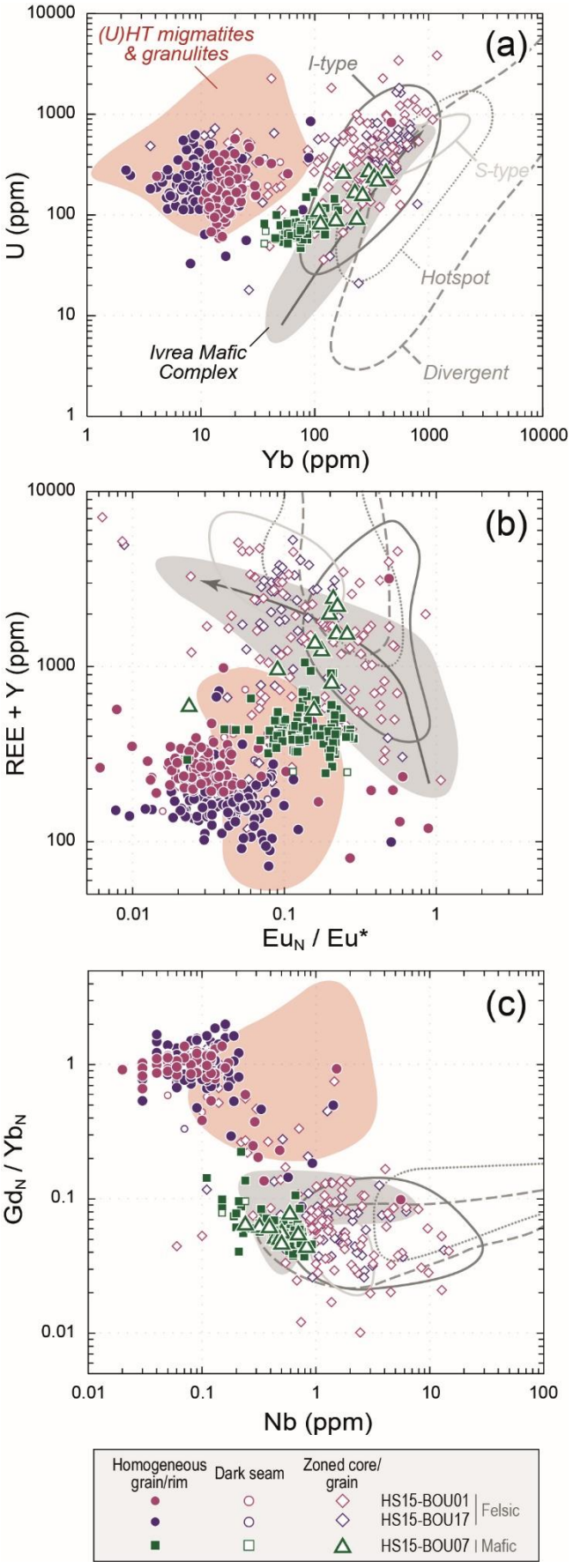
(a)
(U)HT migmatites & granulites
I-type
S-type
Hotspot
Divergent
Ivrea Mafic Complex
U (ppm)
Yb (ppm)
10000
1000
100
10
1
1
10
100
1000
10000
(b)
REE + Y (ppm)
Eu$_N$ / Eu*
0.01
0.1
1
(c)
Gd$_N$ / Yb$_N$
Nb (ppm)
0.01
0.1
1
10
100
Homogeneous grain/rim
Dark seam
Zoned core/ grain
HS15-BOU01
HS15-BOU17
Felsic
HS15-BOU07
Mafic

Figure 7

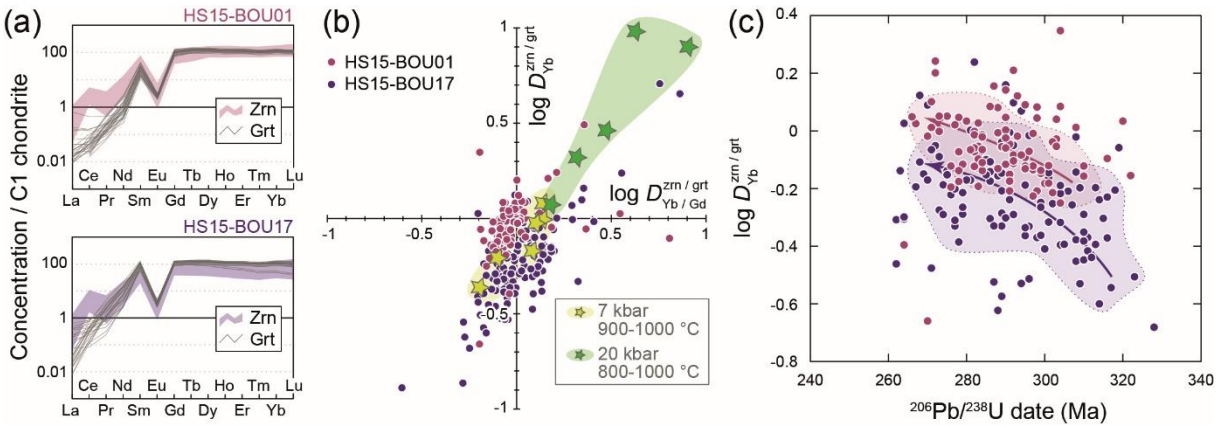
(a)
HS15-BOU01
HS15-BOU17
Zrn
Grt
Concentration / C1 chondrite
100
1
0.01
Ce Nd Eu Tb Ho Tm Lu
La Pr Sm Gd Dy Er Yb
(b)
HS15-BOU01
HS15-BOU17
log $D^{zrn/grt}_{Yb}$
log $D^{zrn/grt}_{Yb/Gd}$
7 kbar
900-1000 °C
20 kbar
800-1000 °C
(c)
log $D^{zrn/grt}_{Yb}$
$^{206}Pb/^{238}U$ date (Ma)

Figure 8

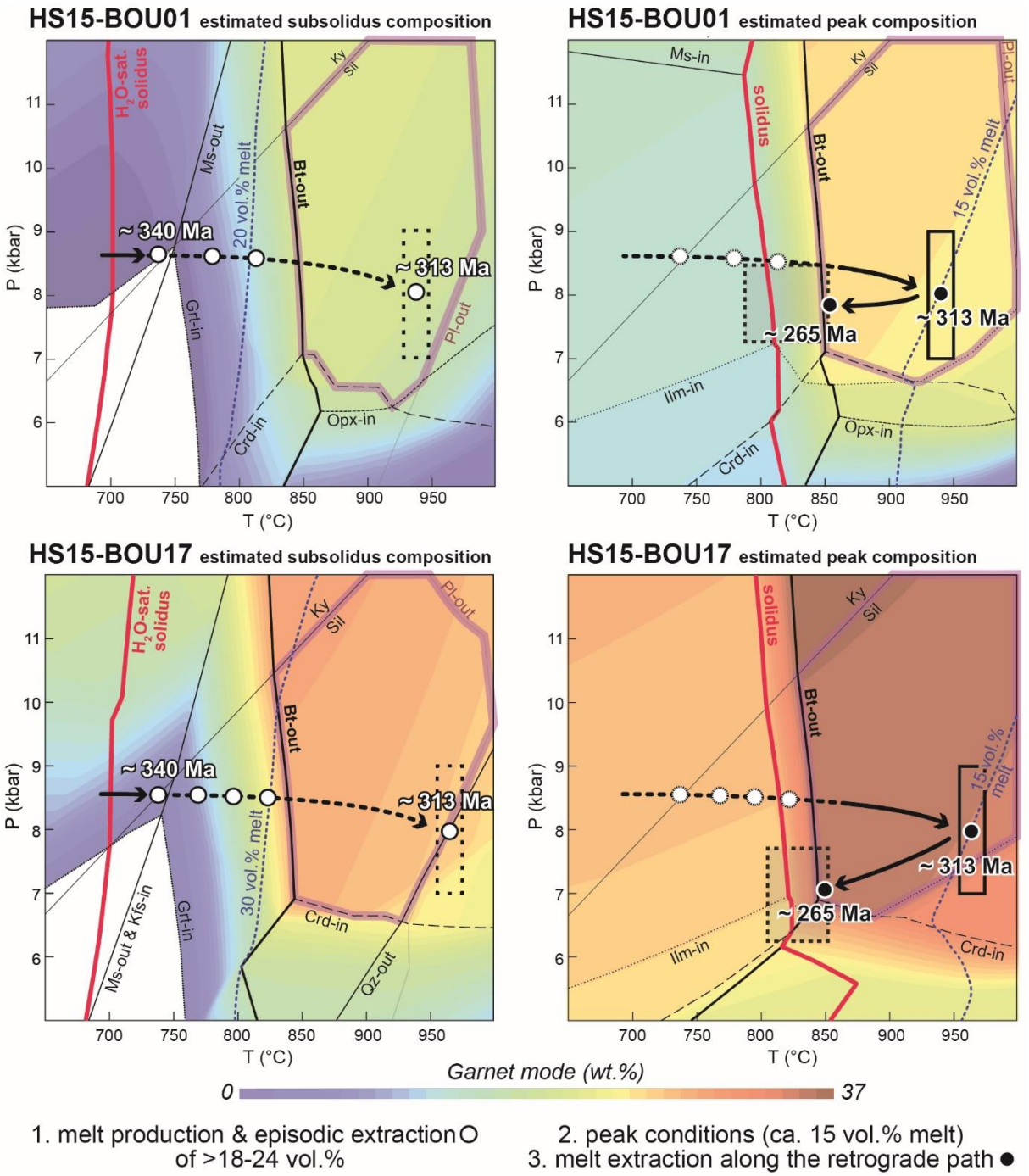
HS15-BOU01 estimated subsolidus composition
HS15-BOU01 estimated peak composition
HS15-BOU17 estimated subsolidus composition
HS15-BOU17 estimated peak composition
H2O-sat. solidus
solidus
Ms-out
Ms-in
Bt-out
Ky
Sil
Pl-out
Grt-in
Crd-in
Opx-in
Ilm-in
Ms-out & Kfs-in
Qz-out
20 vol.% melt
30 vol.% melt
15 vol.% melt
~ 340 Ma
~ 313 Ma
~ 265 Ma
P (kbar)
T (°C)
Garnet mode (wt.%)
0
37
1. melt production & episodic extraction of >18-24 vol.%
2. peak conditions (ca. 15 vol.% melt)
3. melt extraction along the retrograde path

Figure 9

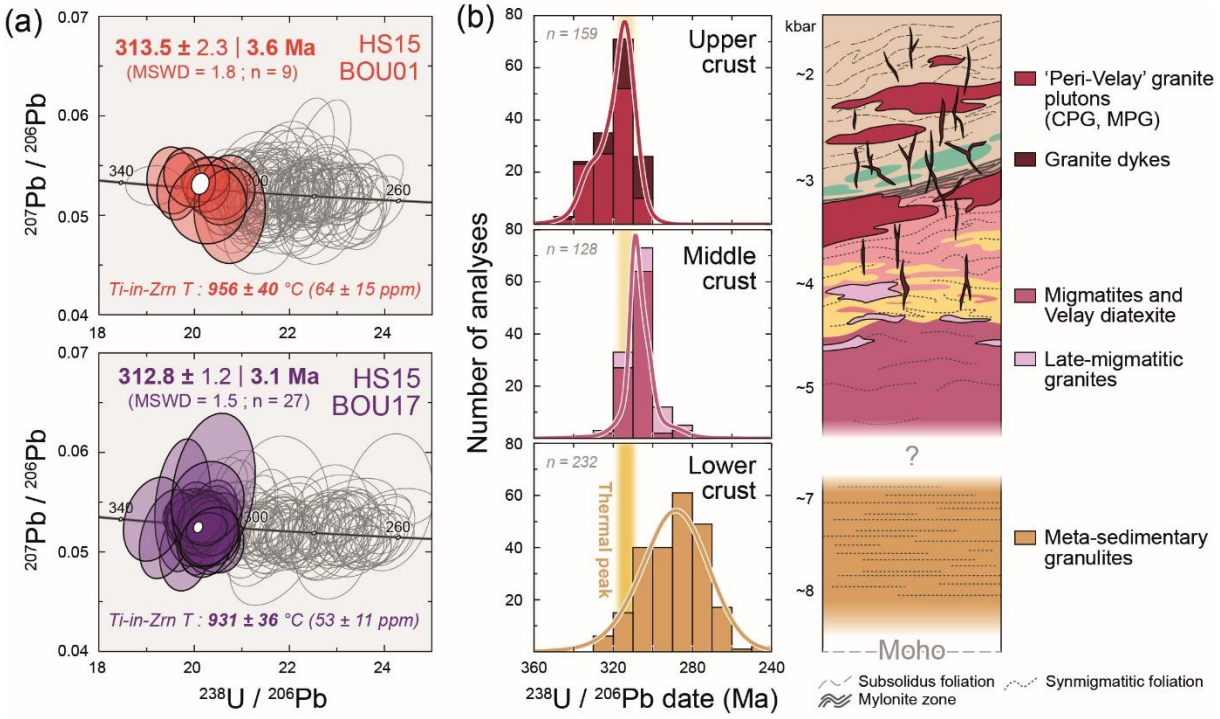
(a)
313.5 ± 2.3 | 3.6 Ma
(MSWD = 1.8 ; n = 9)
HS15
BOU01
Ti-in-Zrn T : 956 ± 40 °C (64 ± 15 ppm)
312.8 ± 1.2 | 3.1 Ma
(MSWD = 1.5 ; n = 27)
HS15
BOU17
Ti-in-Zrn T : 931 ± 36 °C (53 ± 11 ppm)
207Pb / 206Pb
238U / 206Pb
(b)
n = 159
Upper crust
n = 128
Middle crust
n = 232
Lower crust
Thermal peak
Number of analyses
238U / 206Pb date (Ma)
kbar
~2
~3
~4
~5
~7
~8
?
Moho
'Peri-Velay' granite plutons (CPG, MPG)
Granite dykes
Migmatites and Velay diatexite
Late-migmatitic granites
Meta-sedimentary granulites
Subsolidus foliation
Synmigmatitic foliation
Mylonite zone

Figure 10